ABSTRACT

MADHAVAN, SRIKRISHNAN. An Efficient approach for Two Scale Modeling of Seismic Soil Structure Systems. (Under the direction of Dr. Murthy N. Guddati.)

An efficient approach to model seismic soil structure interaction is developed where the soil is horizontally stratified and the system is located away from the seismic source. The approach involves (a) obtaining the free-field solution using deconvolution consistent with the discretization of the local domain, (b) global to local information transfer via a scattering formalism that incorporates absorbing boundaries and (c) utilizing Complex-length Finite Element Method (CFEM) for the local region to reduce the discretization size and thus the overall computational cost. The fundamental idea behind CFEM is that the large computational cost associated with modeling large soil layers is significantly reduced by focusing only on the solution on the edges of the layers, since the response is needed for the building, and not inside the layers. The proposed approach is implemented for both anti-plane shear and plane strain, illustrating that the proposed approach requires minimal modification to existing finite element codes and results in significant reduction in the computational cost. The method can easily be extended to 3D settings where the computational cost reduction is expected to be much more significant.

An Efficient approach for Two Scale Modeling of Seismic Soil Structure Systems

by
Srikrishnan Madhavan

A thesis submitted to the Graduate Faculty of
North Carolina State University
in partial fulfillment of the
requirements for the degree of
Master of Science

Civil Engineering

Raleigh, North Carolina

2016

APPROVED BY:

_____	_____
Dr. Murthy Guddati Committee Chair	Dr. Shamimur Rahman
_____	
Dr. Michael Borden	

DEDICATION

To my parents, teachers, friends and well-wishers

BIOGRAPHY

Srikrishnan Madhavan, son of Rajagopalan Madhavan and Usha Madhavan was born and brought up in the city of Chennai, Tamilnadu, India. He completed his undergraduate degree of Bachelor's in Civil Engineering at National Institute of Technology, Tiruchirappalli during May 2014. He then joined North Carolina State University to pursue his Masters in Civil Engineering specializing in the Structural Engineering. The following thesis is a result of the research conducted during this period.

TABLE OF CONTENTS

LIST OF TABLES

LIST OF FIGURES

1 INTRODUCTION

Modeling of problems where a small scale system is present and interacting with a much larger system forms a broad class of two-scale problems. The size difference and complexity of interaction entails that such systems do not easily conform to simplistic methods of analysis. In the context of dynamic soil-structure interaction (SSI) modeling subjected to earthquakes, the layered geotechnical site forms the global system. On the other hand, the system of interest, such as a building or a tunnel, with nearby irregularities forms the smaller scale local system. The goal of this thesis is to address this problem of two-scale soil structure interaction in order to estimate the structural response with an inherent assumption of the seismic source being far away from the system.

1.1 Review of existing methods

The effect of seismic ground motion on structures has quite an extensive literature (1). The full problem involves characterization of fault source (2), the wave propagation through the soil layers and its eventual effect on the structure. While significant research is being done on the first two aspects by seismologists, the significance of the effects of soil onto the structure via their interaction is the focus of structural and geotechnical earthquake engineers. The early analysis generally ignored the effect of Soil-Structure interaction citing that the effects only diminished the response. Further studies, for example (3), discussed the role of SSI in seismic response of the structure. It establishes that the effects do exist due to soil-layers and that indiscriminate simplifications should not be used. The famous 1985 Mexico City and 1989

Loma Prieta earthquakes were crucial in establishing the significance of local site effects on the soil response as illustrated in (4).

To account for the SSI effects, methods involving superposition of responses were developed. First the site response is obtained which is then used to obtain the structural response. In this context, 1D and/or 2D site response estimation techniques serve as the starting point for SSI analysis (1). These involve developing synthetic seismograms to predict ground motion or using recorded free field ground motion which can then be deconvoluted to obtain the entire site response. For example, reference (5) provides a blind deconvolution method to obtain the site response characteristics. Other studies such as (6) and (7) compare different site response analysis methods as well as ways to obtain the fundamental period of a soil site consisting of multiple soil layers.

Simple analytical methods were developed to analyze for the coupled response of the site and structure (8). 1D methods of analysis were used in both frequency and time domains (e.g. (9)), but they suffer from being simplistic approximations especially in case of structures embedded into the soil. Studies such as (10) indicate that SSI effects are crucial to buildings and outlined the need for an improved procedure of SSI analysis. The significance of finite element based 2D SSI analysis, and how it compares with a simplistic 1D model, is presented in (11). Another aspect is the use of absorbing boundaries. While some studies used viscous dashpots and springs, others include the use of infinite elements (e.g. (12)). These illustrate the need to have a 2D/3D setting with accurate and efficient absorbing boundaries in order to capture the complex responses arising due to SSI.

With this in mind, some approaches in SSI analysis include semi-analytical methods such as (13), but they apply to ground motions with the source near to the site. But this thesis deals with SSI analysis when the causative fault is far away from the site. Studies such as (14) highlight the differences in response when analyzing near-fault and far-fault SSI systems. In general finite-element based SSI analysis uses direct or sub-structure methods (1). Direct methods involve modeling the entire region along with the site and the causative fault. Using direct methods in 2D or 3D setting necessitates the need for significant computational effort to simulate the soil-structure interaction problem (e.g. (15)). For our case, when the earthquake originates at an unknown location far away from the site, and characterization of the propagation path is unknown, utilizing direct methods renders modeling the entire region infeasible.

In this context substructure based methods subdivide the problem into sub-problems (16) where the site response estimation is decoupled from the soil-structure interaction analysis. Computer programs based on this method such as SASSI (17) are utilized but are limited to a linear local site. For example, studies carried out in (18) used SASSI which assumes the linearity of soil for sub-structuring. The study went on to highlight the need to represent local soil non linearity in the context of SSI. Also (19) illustrated how for massive nuclear power-plant structures resting on multi-layered soil, surface response and embedded structure response can have significant differences. Other comprehensive studies such as those conducted by (20) and (21) illustrate the extent of response modification under soil structure interaction and outline the need for improved numerical prediction of SSI effects.

An improvement over this, provided by (22), is the Domain Reduction Method (DRM), which restricts the problem to the local domain but requires an explicit boundary layer around that domain. The method proposed in (23) utilizes a procedure similar to DRM, but without the dependency on the boundary layer and instead uses a stiffness consistent traction in the formulation. However, it does not address the computational cost issue that enters due to the discretization of large soil layers. The importance of efficiently solving the soil-structure interaction problem is further highlighted in a 3D setting with embedded structures such as tunnels (see e.g. (24), (25)). To address issues of computational cost, a transformation based approach was suggested in (26). Hybrid-methods to reduce computational cost were also developed e.g. in (27) but they have increased complexity.

1.2 Response Estimation Away from the Source

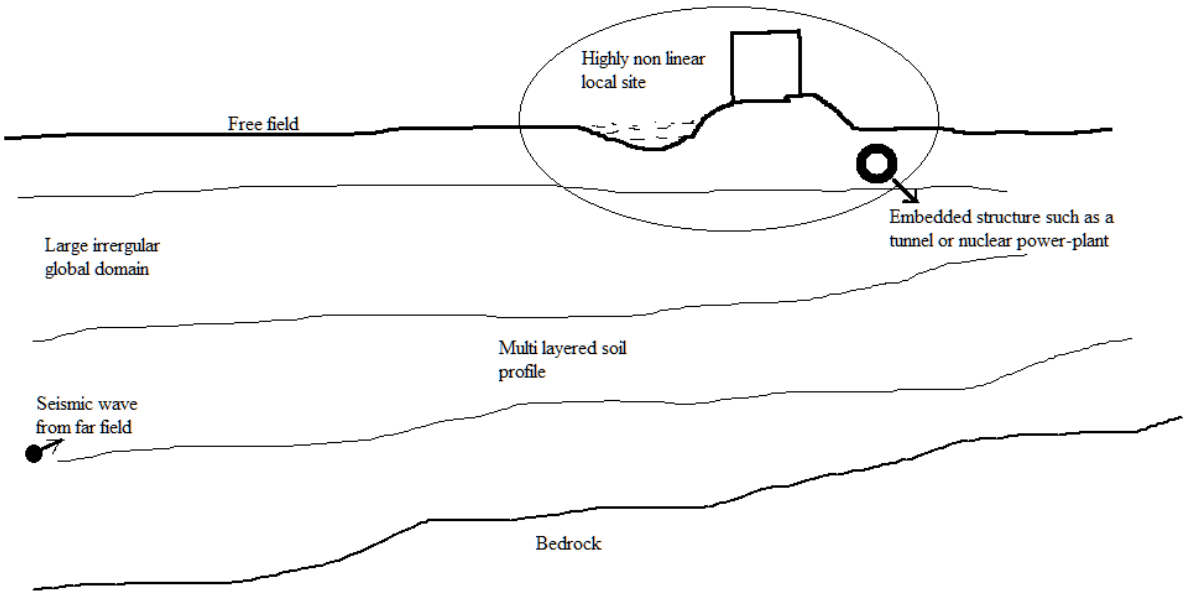

Figure 1-1 General schematic depicting two scale seismic soil structure system viewed from a basin level

One of the critical factors in seismic response estimation away from the source is that, due to unknown magnitude, directivity and properties of the seismic wave, there is a need to rely on ground motion records. Databases such as those provided by PEER and USGS, provide valuable starting points to assess the nature of earthquake occurring in the region. Many ground response estimation techniques utilize the recorded ground motions at the surface to arrive at bedrock motions using approaches such as deconvolution. We follow a similar approach in this thesis.

Specifically, we assume that we have the ground motion at the surface and the knowledge of the local site profile, i.e. the geometry and material properties that can be obtained using geologic soil profiling or other subsurface investigation technique.

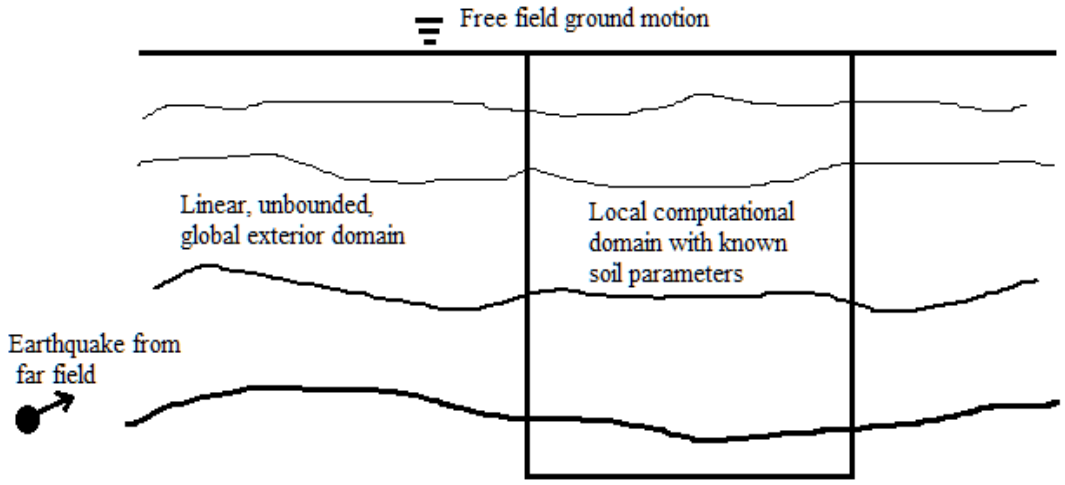

Figure 1-2 Description of reduced local domain in context of seismic input from far field

1.3 Assumptions used in the model

For a soil structure system set far away from the source, the free field ground motion is obtained from recorded data and the spatial variation of ground motion in that region is lost. This implies that in the worst case, a local region has to rely on the recorded data obtained from just one seismogram. The incident wave then, has to be assumed to be only a function of depth and spatially invariant in other directions. Such an assumption can be justified by the fact that top soil layers are slower than the deeper layers making the earthquake waves bend vertically as they enter the top layers (Snell's law).

Yet another assumption inherent in this analysis is that of a linear, unbounded global domain. The geotechnical site is assumed to be a horizontally layered, semi-infinite half-space that is linear and homogenous in the direction of unboundedness.

1.4 Schematic of the soil-structure problem

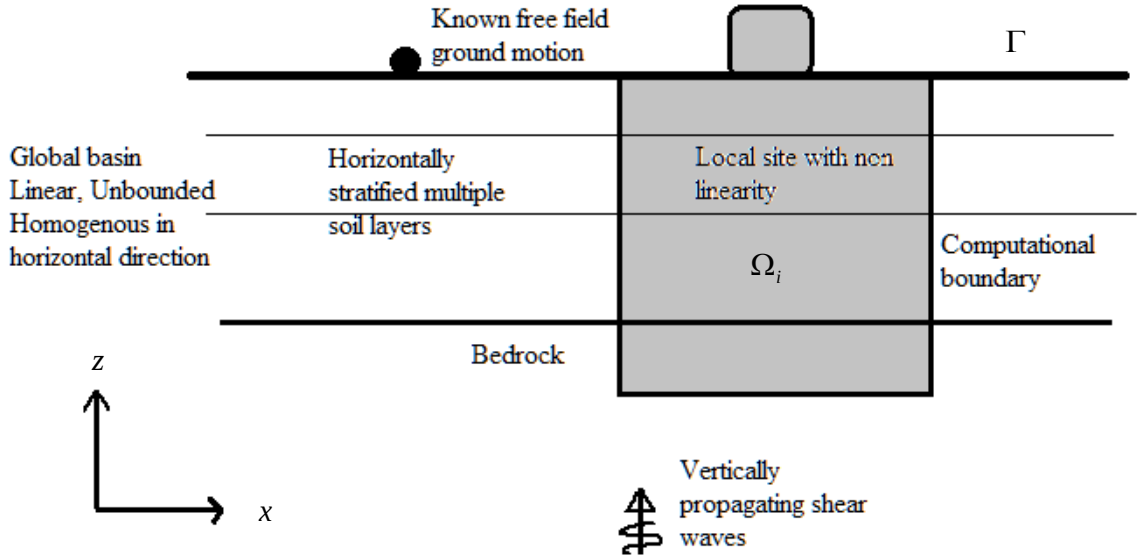

Figure 1-3 Schematic of the reduced model problem

The goal is to determine the response of the soil structure system shown in Figure 1-3. The governing equations for anti-plane shear are given; plane strain equations are similar, albeit more complicated. In the interior Ω_i,

$$-\frac{\partial}{\partial x}\left(G\frac{\partial u}{\partial x}\right)-\frac{\partial}{\partial z}\left(G\frac{\partial u}{\partial z}\right)-\rho\omega^2 u = f. \tag{1.1.1}$$

Traction on the free surface is given by the homogenous Neumann boundary condition,

$$G\frac{\partial u}{\partial \mathbf{n}} = 0. \tag{1.1.2}$$

Radiation boundary condition is applicable in the exterior.

1.4.1 Problem statement:

The focus of this thesis is to provide an efficient way to solve for the responses, in the frequency domain of a 2D/3D soil structure system set far away from the source, subjected to vertically propagating shear waves, where a non-linear local site with the structure of interest interacts with the surrounding global site that is assumed linear, horizontally stratified and homogenous in the direction of unboundedness. While the method developed here can be extended to three-dimensional settings, the scope of the thesis is limited to two-dimensional settings, i.e. anti-plane shear and plane strain.

1.5 Issues with existing approaches – computational cost

In general, the size and scale of the soil-structure system is large. The depth to bedrock of a multilayered soil profile can be as large as 50 – 100m. On the other hand, the finite elements used in the model must be fine enough to capture waves propagating in a layer with the shortest

wavelength for the largest expected frequency. This often means that the associated computational cost becomes huge. One way to deal with this would be to use a graded mesh that is dependent on the wave velocity in a layer for the largest expected frequency. Even then, a large number of layers implies that computational cost becomes a bottleneck. For example, a parametric study conducted for the simple case of a 2D structure resting on a three-layered soil under anti-plane shear, revealed that for a target error of 1%, the FE model required 120 elements in the vertical direction. Extrapolating this to a 3D problem with 100 elements in each horizontal direction it would require more than 1.2 million elements. If it were to include a general 3D elastodynamic problem with more than 5 soil layers the amount of FE required would be prohibitively expensive. With this in mind, an efficient method of modeling the layered soil-structure system is proposed building from the formalism developed in (23).

The organization of the thesis is as follows. Chapter 2 discusses the key concepts currently employed for the analysis of global-local SSI problem and a tool that can increase efficiency. Chapter 3 outlines how the proposed efficiency can be included consistently with the existing approach. Chapter 4 presents some numerical examples illustrating its usage and a discussion of results and Chapter 5 includes the summary with conclusions and recommendations for future work.

2 PRELIMINARIES

This chapter illustrates three key ideas that will be used in the proposed solution methodology.

1) The Crank-Nicolson (CN) method
2) Perfectly Matched Discrete Layers (PMDL)
3) Complex Finite Elements (CFEM)

The concepts are presented in a stand-alone fashion in this chapter to aid in understanding of the overall formulation presented in the next chapter.

2.1 The Crank Nicolson Method

For a one-dimensional partial differential equation of the form,

$$\frac{\partial \mathbf{p}}{\partial z} = \mathbf{F}(z), \tag{2.1.1}$$

the Crank-Nicolson finite difference approximation takes the form

$$\frac{\mathbf{p}^{n+1} - \mathbf{p}^{n}}{\Delta z} = \frac{1}{2}\left[\mathbf{F}^{n+1}(z) + \mathbf{F}^{n}(z)\right], \tag{2.1.2}$$

where $\mathbf{p}$ and $\mathbf{F}$ are vector field variables and Δz the element length.

2.1.1 Crank Nicolson Method for 1D Wave Propagation

Consider a vertically propagating shear wave, in a half-space with shear wave velocity c_s, shear modulus G and an angular frequency of ω.

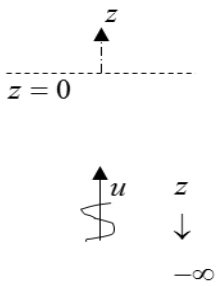

Figure 2-1 Vertically propagating 1D shear wave

The governing differential equation can be written as:

$$\frac{\partial^2 u}{\partial z^2} + \left(k_z\right)^2 u = 0, \tag{2.1.3}$$

$$G\frac{\partial u}{\partial z}\bigg|_{z=0} = 0, \tag{2.1.4}$$

where,

$$k_z = \frac{\omega}{c_s}. \tag{2.1.5}$$

From the stress-strain constitutive equations, we have:

$$\tau = G\frac{\partial u}{\partial z}, \tag{2.1.6}$$

where, u is the displacement wave field and τ is the shear stress.

Substituting (2.1.6) in (2.1.3) gives,

$$\frac{\partial \tau}{\partial z} + G\left(k_z\right)^2 u = 0. \tag{2.1.7}$$

Rewriting (2.1.6) gives,

$$\frac{\partial u}{\partial z} - \frac{\tau}{G} = 0. \tag{2.1.8}$$

Combining equation (2.1.7) and (2.1.8) results in

$$\frac{\partial}{\partial z}\begin{Bmatrix} u \\ \tau \end{Bmatrix} + \begin{bmatrix} 0 & -\dfrac{1}{G} \\ G\left(k_z\right)^2 & 0 \end{bmatrix}\begin{Bmatrix} u \\ \tau \end{Bmatrix} = \begin{Bmatrix} 0 \\ 0 \end{Bmatrix}. \tag{2.1.9}$$

This is similar to Equation (2.1.1),

$$\frac{\partial}{\partial z}\mathbf{p} + \mathbf{A}\mathbf{p} = 0, \tag{2.1.10}$$

where $\mathbf{p} = \begin{Bmatrix} u \\ \tau \end{Bmatrix}$ and

$$\mathbf{A} = \begin{bmatrix} 0 & -\dfrac{1}{G} \\ G\left(k_z\right)^2 & 0 \end{bmatrix}. \tag{2.1.11}$$

Using Crank-Nicolson method in Equation (2.1.10), we have,

$$\frac{\mathbf{p}^{n+1} - \mathbf{p}^n}{\Delta z} = -\frac{1}{2}\mathbf{A}\left[\mathbf{p}^{n+1} + \mathbf{p}^n\right]. \tag{2.1.12}$$

Rewriting this equation provides,

$$\left[\frac{1}{\Delta z}\mathbf{I_2} + \frac{1}{2}\mathbf{A}\right]\mathbf{p}^{n+1} = \left[\frac{1}{\Delta z}\mathbf{I_2} - \frac{1}{2}\mathbf{A}\right]\mathbf{p}^n. \tag{2.1.13}$$

This is the Crank-Nicolson propagator equation as it facilitates the propagation of the vector $\mathbf{p}$ from $z = z_0$ to $z = z_{n+1}$.

$\mathbf{p}^0 = \begin{Bmatrix} u_0 \\ \tau_0 \end{Bmatrix}$ is the initial value specified at $z = z_0$, and recursive application of Equation (2.1.13) results in the displacements and tractions at all the desired depths z_i .

2.1.2 Crank Nicolson Method for 2D wave propagation

When the waves propagate obliquely, the formalism described above would still be valid, due to Snell's law that states that the horizontal wavenumber is invariant through the depth. Thus, the wave-field can be split into multiple harmonics in the x direction, and Crank-Nicolson method is applicable after performing Fourier transform in the x direction. The associated equations are summarized below.

For in-plane waves with angular frequency ω, Lamé constants λ and μ, density ρ and horizontal wavenumber k_x, when written in first order form gives:

$$\frac{\partial}{\partial z}\mathbf{p} + \mathbf{A}\mathbf{p} = 0, \tag{2.1.14}$$

where, $\mathbf{p} = \begin{Bmatrix} u_x \\ u_z \\ \tau_{xz} \\ \sigma_{zz} \end{Bmatrix}$ is a function of (z, ω), and $\mathbf{A}$ is given by,

$$\mathbf{A} = \begin{bmatrix} 0 & ik_x & -\frac{1}{\mu} & 0 \\ \frac{\lambda i k_x}{\lambda + 2\mu} & 0 & 0 & \frac{-1}{\lambda + 2\mu} \\ \rho\omega^2 - \frac{4k_x^2\left(\mu^2 + \lambda\mu\right)}{\lambda + 2\mu} & 0 & 0 & \frac{\lambda i k_x}{\lambda + 2\mu} \\ 0 & \rho\omega^2 & ik_x & 0 \end{bmatrix}. \tag{2.1.15}$$

The marching equation takes the form,

$$\left[\frac{1}{\Delta z}\mathbf{I_4} + \frac{1}{2}\mathbf{A}\right]\mathbf{p}^{n+1} = \left[\frac{1}{\Delta z}\mathbf{I_4} - \frac{1}{2}\mathbf{A}\right]\mathbf{p}^{n}. \tag{2.1.16}$$

After computing $\mathbf{p}$ at any depth, the remaining stress component, namely σ_{xx} can be determined using the equation,

$$\sigma_{xx} = \frac{1}{\lambda + 2\mu}\left(\lambda\sigma_{zz} + 4ik\left(\mu^2 + \lambda\mu\right)u_x\right). \tag{2.1.17}$$

2.1.3 Crank Nicolson Method for SSI Problem

The Crank-Nicolson method can be used as a method of deconvolution of free field motion to obtain the ground motion throughout the depth. Deconvolution is the process of using Initial values of stresses and displacements at the free field and the stiffness of the soil layer to obtain the ground motion at a depth. In a discrete system, this involves obtaining the propagator matrix and marching through the depth to obtain the deconvoluted field values. The Crank Nicolson method is one such propagator method. The effectiveness of the CN method in this context is further discussed in Section 3.5.2.

2.2 Perfectly Matched Discrete Layers (PMDL)

PMDL is an absorbing boundary condition developed in the past decade (see e.g. (28)) aimed at capturing the effect of unbounded exteriors, such as those encountered in the SSI problem. The idea is that the stiffness of the bottom half space is approximated with just a handful of PMDL layers on the computational boundary. While the details of PMDL can be found in (29), in the reminder of this section, we provide a basic summary of PMDL.

2.2.1 The idea behind PMDL

Figure 2-2 presents the basic summary of how PMDL approximates the half-space stiffness, in the simpler 1D setting. Figure a) denotes the continuous half-space with an exact stiffness K_{hs} . Adding a single element to the half space with regular integration (say two point) results in K_{system} that does not equal the exact half-space stiffness, due to finite element discretization error. However, utilizing midpoint integration to evaluate the system matrices eliminates the discretization error and the resulting system stiffness exactly equals the half-space stiffness (29). The crucial point to note is that the half-space impedance is recovered irrespective of element length. The next step is to recursively replace the unbounded domain with midpoint-integrated elements. To keep the system finite, truncation is introduced after some elements. Due to truncation an error is introduced into the system stiffness. The length of the elements (PMDL parameters) are chosen so as to minimize this error. It turns out that in the context of wave propagation, reducing the error requires complex element lengths, similar to the celebrated method of perfectly matched layers (PML), (see (30), (31)). A specific approach to choose the PMDL element lengths is presented in (29) and summarized below:

$$L_j = \frac{-2ic_j}{\omega}, \tag{2.2.1}$$

where

$$c_j = \frac{c}{\cos\left(\frac{(j-1)}{2n}\pi\right)}, \qquad j:1\to n. \tag{2.2.2}$$

L_j : Length of the j^{th} element
n : Number of PMDL elements used
ω : Frequency in radians per second
c : Wave velocity

Based on numerical experiments in (29), around 3-5 PMDL layers are sufficient, to approximate the half space stiffness with a high degree of accuracy.

a) Continuous half-space

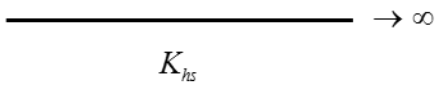

b) One element with regular integration + half-space

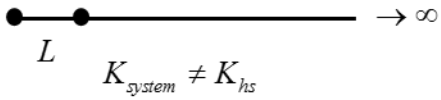

c) One element with mid point integration + half-space

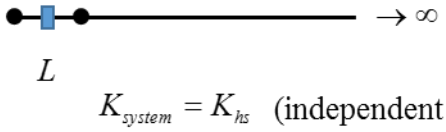

d) Recursive replacement with mid point integrated PMDL elements with truncation

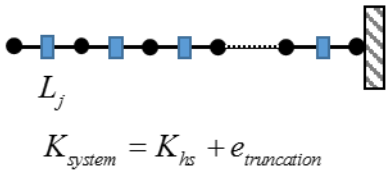

e) Length of each element chosen so as to minimize truncation error

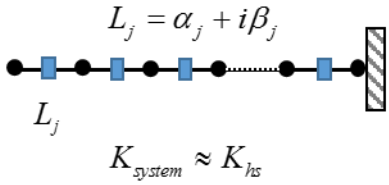

Figure 2-2 Illustration of PMDL approximating half-space stiffness

2.2.2 PMDL for 2D mesh

For a 2D domain, the PMDL mesh for the edges is the product of regular FEM discretization along the boundary and 1D PMDL discretization perpendicular to the boundary. On the other hand, at the corners, the PMDL mesh consists of tensor product of two 1D PMDL discretization perpendicular to each of the two edges meeting at the corner (see (29)). A typical 2D mesh is shwon in Figure 2-3.

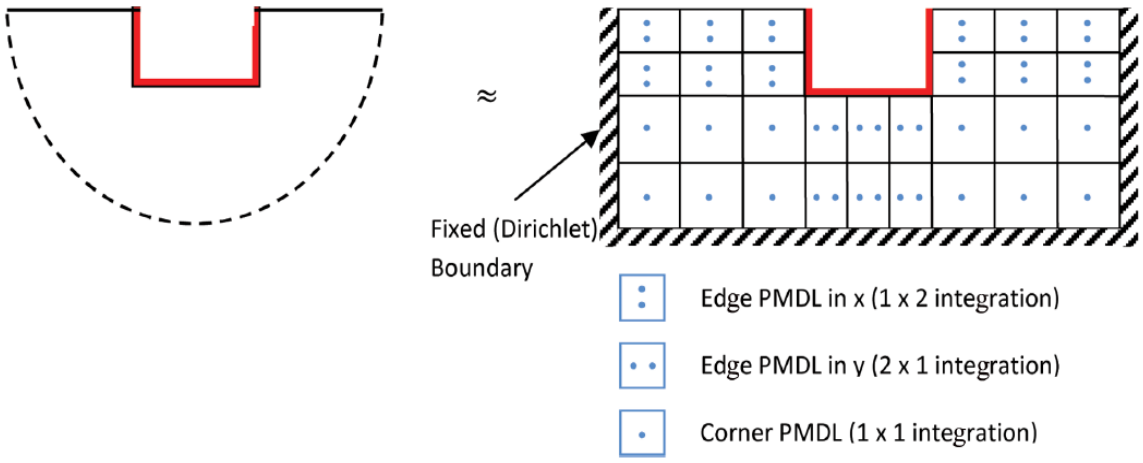

Figure 2-3 PMDL approximation of exterior in 2D along with integration points (23)

2.2.3 PMDL for the SSI problem

The reduced problem of soil structure interaction consists of horizontally stratified medium with the outer domain being homogenous and unbounded for each layer in the horizontal direction and a half-space of bedrock extending infinitely below.

This natural structure lends itself well to application of PMDL as it can be used on the left and right side of the domain, as well as the bottom half-space that represents the bedrock. More detailed information on PMDL can be found in references (28, 29, 32)

2.3 Complex-Length Finite Element Method

Complex-length Finite Element Method (CFEM) is a method to obtain the response at select localized regions, whereby the discretization along with nature of integration is modified so as to have exponential convergence at preselected points. In the case of layered subdomains, usage of CFEM inside the layer results in exponential convergence at the layer boundaries. While further details can be found in (33), a brief summary is given in the rest of the section.

2.3.1 Summary of CFEM

1) The mesh is bent into complex plane with specific lengths that are in complex conjugate pairs. Few complex finite elements are sufficient to achieve a high degree of accuracy. The choice of lengths are presented in Section 2.3.3
2) The elements are mid-point integrated along the direction of complex mesh bending.

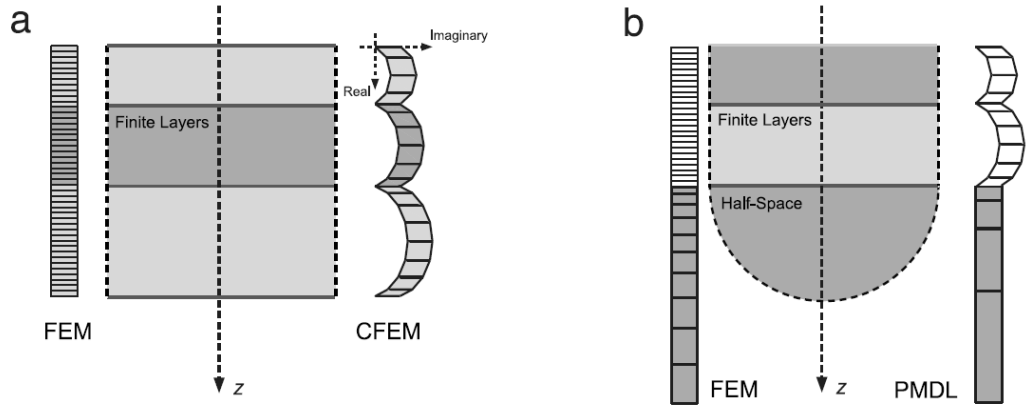

Figure 2-4 Illustration of FEM vs CFEM - Mesh Bending (34)

The key advantages are:

1) The solution at layer boundaries is obtained accurately with just few Complex-length finite elements compared to a large number of conventional finite elements.

2) The lengths of the CFEM elements scale with the length of the layer and are independent of the domain properties or the frequency (as in contrast with PMDL).

It must be pointed out that we do not obtain the response *inside* the layer modeled with CFEM, which is the price we pay for obtaining exponential convergence at the layer boundaries.

2.3.2 The idea behind CFEM

For a 1D Helmholtz equation of the form

$$-\frac{\partial^2 u}{\partial x^2} - \omega^2 u = 0, \quad x \in [0, L], \tag{2.2.3}$$

where $\omega \in \mathbb{R}$ denotes the temporal frequency and u is the displacement. The exact stiffness or the Dirichlet-to-Neumann (DtN) map $u\big|_{x=0,L} \rightarrow (du/dx)\big|_{x=0,L}$ is given by,

$$\mathbf{K}^{\text{exact}} = \frac{i\omega}{\sinh(i\omega L)} \begin{bmatrix} \cosh(i\omega L) & -1 \\ -1 & \cosh(i\omega L) \end{bmatrix}. \tag{2.2.4}$$

The discretization is such that, with *mid-point integration and specially chosen complex valued lengths,* for the Dirichlet-to-Neumann (DtN) map exponential convergence is achieved at the surface edges at the expense of solution accuracy in the interior.

2.3.3 Choice of CFE element lengths

If L_j is element size and L the domain size, we can obtain $\frac{L_j}{L} = \frac{2}{x_j}$ where x_j are the roots of the n^{th} degree polynomial given by,

$$\sum_{j=0}^{n} \frac{(2n-j)!}{j!(n-j)!} (-x)^j = 0. \tag{2.2.5}$$

For lengths other than unity the values just scale. Illustrated below is a table of element lengths vs number of CFE elements used in a layer.

$n=1$	1.00000000000000	$n=2$	0.50000000000000 ± 0.28867513459481 *i*
$n=3$	0.28468557688388 ± 0.27159985141630 *i* 0.43062884623222	$n=4$	0.18313248053143 ± 0.23132522602625 *i* 0.31686751946856 ± 0.09488202514221 *i*
$n=5$	0.12803667831541 ± 0.19668213834621 *i* 0.23485450871940 ± 0.12209940763707 *i* 0.27421762593037	$n=6$	0.09489061789607 ± 0.16944514819433 *i* 0.17914640739749 ± 0.12594324946340 *i* 0.22596297470643 ± 0.04614135671779 *i*
$n=7$	0.07338559568636 ± 0.14811940741461 *i* 0.14065739395847 ± 0.12154781833235 *i* 0.18538954553266 ± 0.06776497788782 *i* 0.20113492964499	$n=8$	0.05861791492234 ± 0.13119236974564 *i* 0.11325833004971 ± 0.11445496413908 *i* 0.15337794771885 ± 0.07709430353886 *i* 0.17474580730908 ± 0.02713226173787 *i*
$n=9$	0.04802049907890 ± 0.11752570488080 *i* 0.09316287173966 ± 0.10679717990370 *i* 0.12840441052931 ± 0.08014721079992 *i* 0.15100957026047 ± 0.04281546509628 *i* 0.158805296783284	$n=10$	0.04014472910062 ± 0.10630697796687 *i* 0.07802273616547 ± 0.09940003581225 *i* 0.10881874816902 ± 0.07996015060428 *i* 0.13078256453612 ± 0.05163001172938 *i* 0.14223122202876 ± 0.01782841382104 *i*
$n=11$	0.03412261657800 ± 0.09695789626293 *i* 0.06634486381072 ± 0.09256005182226 *i* 0.09329088025857 ± 0.07811366645707 *i* 0.11386072467713 ± 0.05628616844255 *i* 0.12678425930221 ± 0.02942684799389 *i* 0.131193310746699	$n=12$	0.02940803944815 ± 0.08906181395662 *i* 0.05715192456673 ± 0.08635352530097 *i* 0.08082582076929 ± 0.07545289071966 *i* 0.09976290741316 ± 0.05839885662872 *i* 0.11301395814524 ± 0.03687019624343 *i* 0.11983734965741 ± 0.01259866487095 *i*

Figure 2-5 A table of element lengths with number of CFE elements used

2.3.4 CFEM for SSI problem

In the context of soil-structure interaction (say for a 2D domain) where the soil layers are horizontally stratified and unbounded, we can employ CFEM in the vertical direction for the soil layers that do not contain the structure of interest because,

1) There may be a large number of layers with depths that are significant and conventional FEM would require a large number of elements.

2) We are interested in obtaining the effects of the soil layers on the structure and domain of interest and not the solution in the soil layers themselves.

Consider an example domain consisting of two soil layers (Figure 2-6) where the top layer contains an embedded structure (e.g. a tunnel).

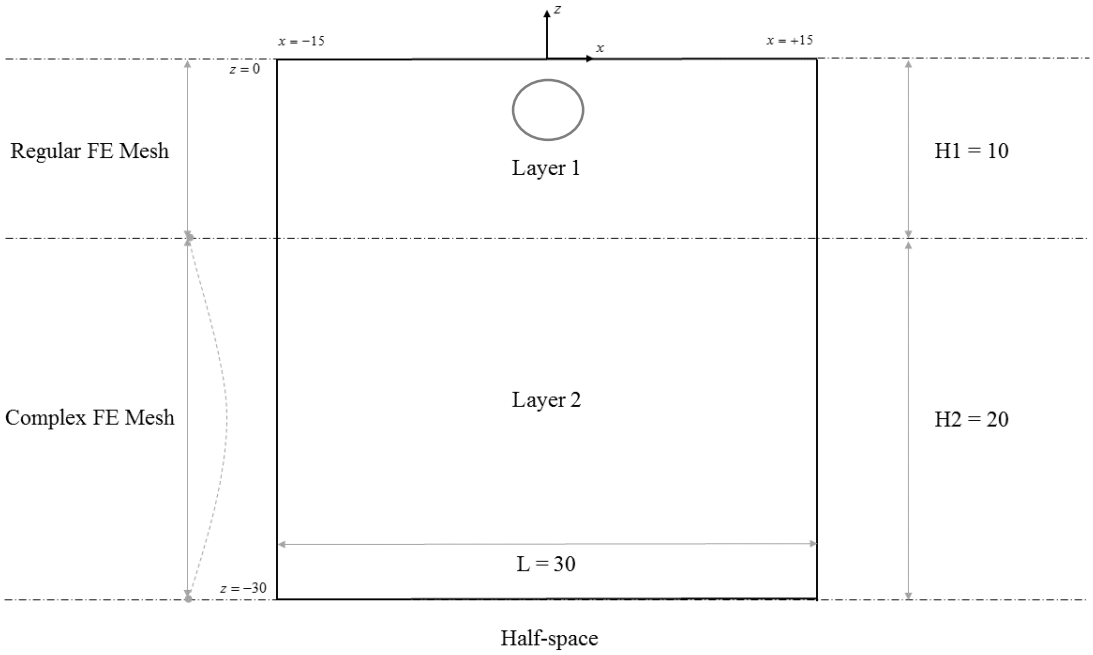

Figure 2-6 Example of soil domain to be discretized

This implies that we can use regular FEM for just the first layer, but replace the second layer with CFE mesh. An illustration of the discretization (of just the domain, without the structure) with 4 elements per unit length for FE and 16 elements for CFEM is given in Figure 2-7. Note the high density of the FE mesh compared to CFEM in the vertical direction.

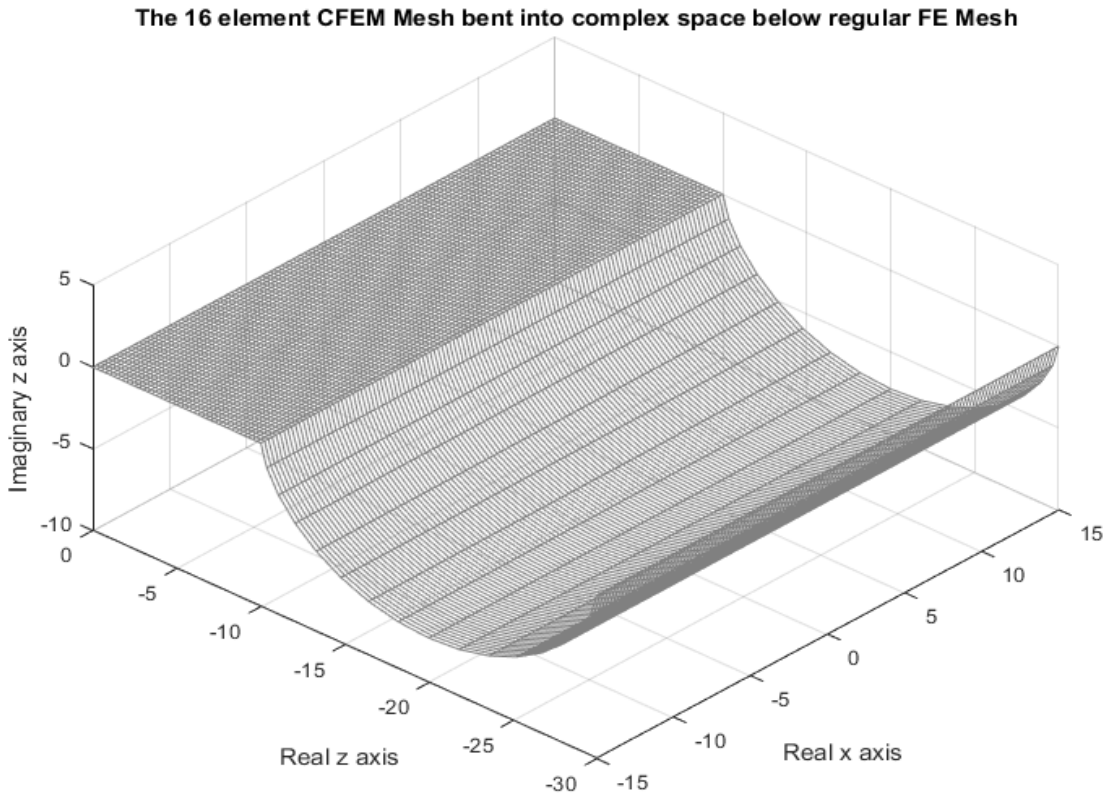

Figure 2-7 3D view of complex CFE bending used for a soil layer

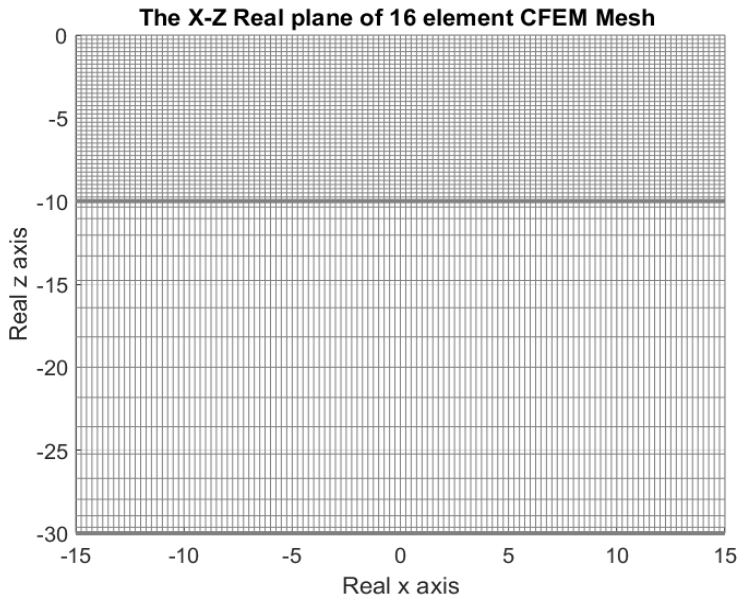

Figure 2-8 Real plane of the discretized soil domain

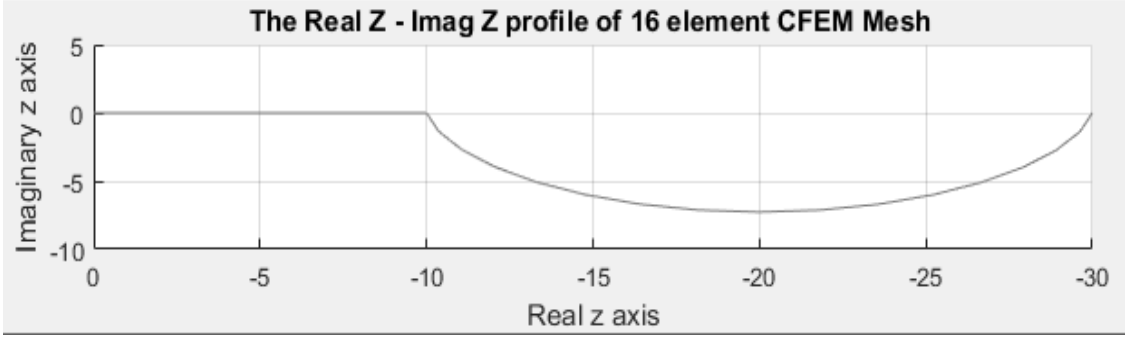

Figure 2-9 Bending of mesh into complex plane

More information regarding the details of the proof and validity of the CFE approach along with its applicability to Laplace, Helmholtz and elastodynamic equations is presented in (33) and (34).

3 PROPOSED APPROACH

The first step is to divide the region into near and far field regions. The near field encompasses the structure and surrounding features which can be non-linear, while the rest of the domain (far field) is linear. The ground motion in the far field is developed from the free-field solution, which is invariant in the horizontal directions but depends on the depth, necessitating a 1D solution procedure (Figure 3-1).

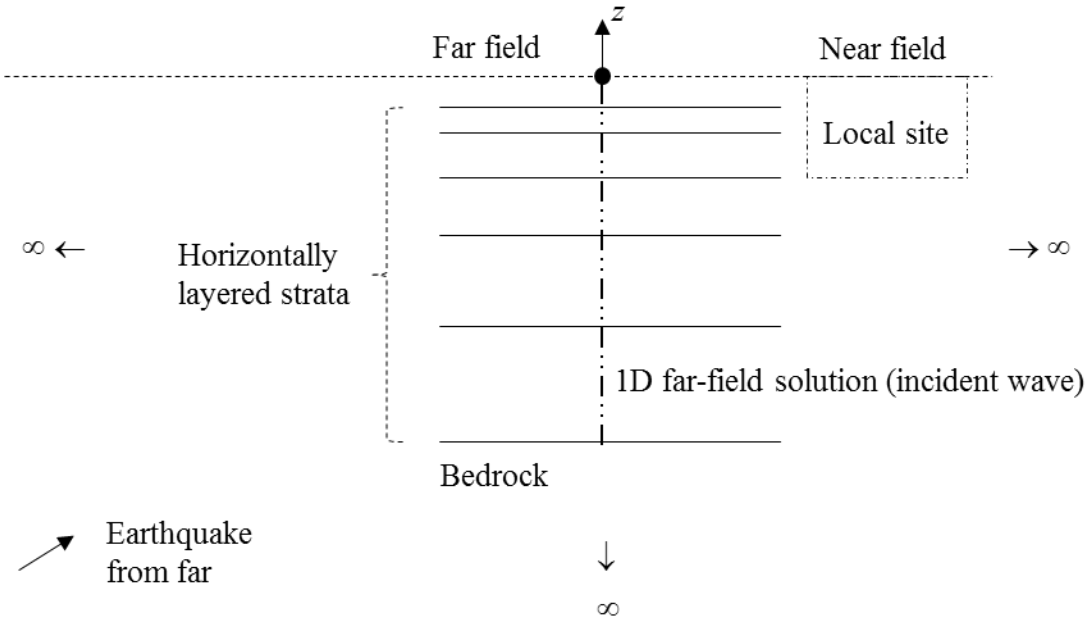

Figure 3-1 1D solution in the far field

The near field, due to irregularities and nonlinearities, typically requires a 2D or 3D FE discretization (see Figure 3-2). The layers where the structure is present is identified and regular FEM is used in the vertical direction for those layers. For the layers that do not contain the structure, CFEM is used in the vertical direction.

The same vertical discretization (along with CFE) is used in the far field to ensure consistent transfer of information between far-field and near-field models. Note that this is applicable for both vertically and obliquely propagating waves. Fourier transform in the horizontal direction is used for the latter case as described in Section 2.1.2; such problems are out of the scope of the present work.

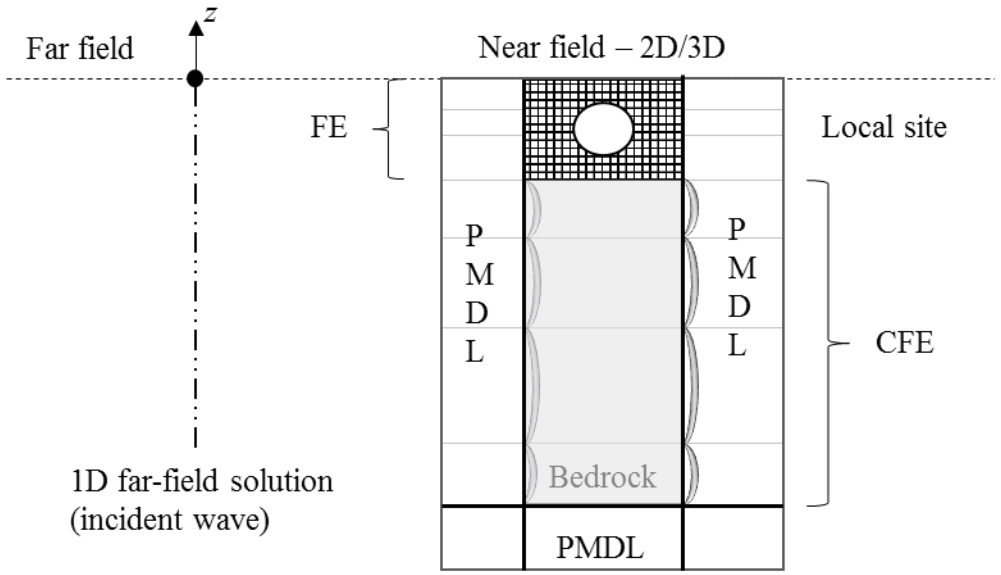

Figure 3-2 2D/3D modeling for the near field

With respect to coupling the far-field and near-field models, due to the complex effects arising from the scattering in the near field, a scattering formalism is employed as described later in this section.

To summarize the main ingredients,

1) A 1D formulation is developed for the far field with vertical discretization consistent with the near field. This formulation is used to obtain the incident displacements and tractions.

2) A 2D/3D near field system is used just for the reduced local domain, along with PMDL to mimic the exterior.
3) CFEM is used in the vertical direction with discretization consistent with near and far-field which makes the system computationally efficient.
4) A scattering formalism is employed to couple the near-field and far-field models.

Below are the details of the stepwise development of the entire approach.

3.1 The continuous problem

Consider a horizontally layered 3D domain that encompasses the near and far field regions. Earthquake excitation is incident from outside of this region.

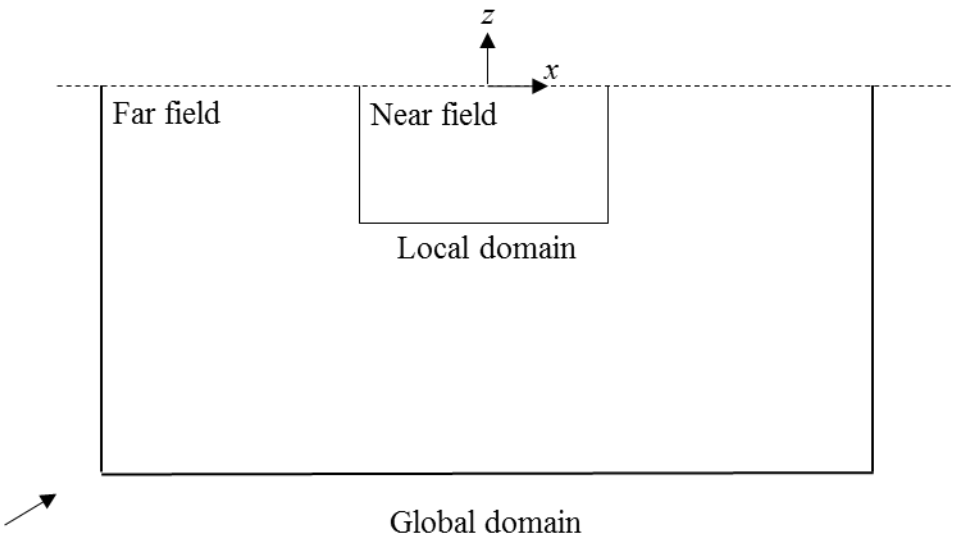

Figure 3-3 Schematic of the general model problem

Wave propagation in linear elastic media is governed by stress equilibrium in three directions. In the absence of body forces, the equation written in the frequency domain is,

$$-\frac{\partial}{\partial x}\begin{Bmatrix}\sigma_{xx}\\ \tau_{xy}\\ \tau_{xz}\end{Bmatrix}-\frac{\partial}{\partial y}\begin{Bmatrix}\tau_{yx}\\ \sigma_{yy}\\ \tau_{yz}\end{Bmatrix}-\frac{\partial}{\partial z}\begin{Bmatrix}\tau_{zx}\\ \tau_{zy}\\ \sigma_{zz}\end{Bmatrix}-\rho\omega^2\begin{Bmatrix}u_x\\ u_y\\ u_z\end{Bmatrix}=0, \tag{3.1.1}$$

where u is the displacement, σ,τ are the stresses, ρ is the density and ω the angular frequency.

Each of the three equations can be written as,

$$\nabla\cdot\boldsymbol{\sigma}_\alpha+\rho\omega^2 u_\alpha=0, \tag{3.1.2}$$

where,

$$\boldsymbol{\sigma}_\alpha=\begin{Bmatrix}\sigma_1\\ \sigma_2\\ \sigma_3\end{Bmatrix}. \tag{3.1.3}$$

u_α and the three components of $\boldsymbol{\sigma}_\alpha$ depend upon the direction of equilibrium Equation (3.1.1) . For example, in the x direction, $u_\alpha=u_x$ and $\boldsymbol{\sigma}_\alpha$ becomes,

$$\boldsymbol{\sigma}_x=\begin{Bmatrix}\sigma_{xx}\\ \tau_{yx}\\ \tau_{zx}\end{Bmatrix}. \tag{3.1.4}$$

Using the weak formulation, Equation (3.1.2) becomes,

$$\int_\Omega \delta u\left(\nabla\cdot\boldsymbol{\sigma}_\alpha+\rho\omega^2 u\right)d\Omega=0, \tag{3.1.5}$$

where $u=u_\alpha$.

3.2 Integration by parts in z followed by Semi-discretization in z direction

The weak form of equation (3.1.5), integrated with respect to z gives:

$$\int_{-H}^{0}\delta u\left(-\frac{\partial}{\partial x}\sigma_1-\frac{\partial}{\partial y}\sigma_2-\frac{\partial}{\partial z}\sigma_3-\rho\omega^2 u\right)dz=0, \tag{3.2.1}$$

where the computational domain (near and far field) has a depth of H in the negative z direction.

Integration by parts in z, i.e.,

$$\int \delta u \frac{\partial}{\partial z} \sigma_3 dz = \left[\delta u \cdot \sigma_3\right] - \int \sigma_3 \frac{\partial \delta u}{\partial z} dz. \tag{3.2.2}$$

Equation (3.2.1) can then be rewritten as,

$$\int_{-H}^{0} \delta u \left(-\frac{\partial}{\partial x}\sigma_1 - \frac{\partial}{\partial y}\sigma_2 - \rho\omega^2 u \right) dz - \left(\left[\delta u \cdot \sigma_3\right]_{-H}^{0} - \int_{-H}^{0} \sigma_3 \frac{\partial \delta u}{\partial z} dz \right) = 0. \tag{3.2.3}$$

Semi-discretization is performed in the z direction for both the local and global domain. PMDL in the z direction is also employed. The following approximation is used for the displacement field.

$$u = \sum_{i=1}^{n} \phi_i(z) u_i(x, y, z, \omega) = \mathbf{\Phi}^T(z) \mathbf{U}(x, y, z, \omega). \tag{3.2.4}$$

Here $\mathbf{\Phi}(z)$ is the basis function vector and $\mathbf{U}(x, y, z, \omega)$ the nodal degrees of freedom vector. Galerkin method is employed in this approximation where the test function takes the same form as the solution given by,

$$\delta u = \sum_{i=1}^{n} \phi_i(z) \delta u_i(x, y, z, \omega) = \mathbf{\Phi}^T(z) \delta \mathbf{U}(x, y, z, \omega) = \delta \mathbf{U}^T \mathbf{\Phi}. \tag{3.2.5}$$

The stress term correspondingly takes the form,

$$\sigma = \sum_{i=1}^{n} \phi_i(z) \sigma_i(x, y, z, w) = \mathbf{\Phi}^T(z) \mathbf{\Sigma}(x, y, z, w). \tag{3.2.6}$$

Using these semi-discretization approximations in (3.2.3) we have,

$$\delta \mathbf{U}^T \left[\int_{-H}^{0} \mathbf{\Phi} \left(-\frac{\partial}{\partial x} \mathbf{\Phi}^T \mathbf{\Sigma}_1 - \frac{\partial}{\partial y} \mathbf{\Phi}^T \mathbf{\Sigma}_2 - \rho\omega^2 \mathbf{\Phi}^T \mathbf{U} \right) dz - \left[\mathbf{\Phi}\mathbf{\Phi}^T \right]_{-H}^{0} \mathbf{\Sigma}_3 + \left(\int_{-H}^{0} \mathbf{\Phi}_z \mathbf{\Phi}^T dz \right) \mathbf{\Sigma}_3 \right] = 0. \tag{3.2.7}$$

which can be written concisely as,

$$\mathbf{A}\left(-\frac{\partial}{\partial x}\boldsymbol{\Sigma}_1 - \frac{\partial}{\partial y}\boldsymbol{\Sigma}_2 - \rho\omega^2\mathbf{U}\right) + \mathbf{B}\left(\boldsymbol{\Sigma}_3\right) = 0, \tag{3.2.8}$$

Where,

$$\mathbf{A} = \int_{-H}^{0} \boldsymbol{\Phi}\boldsymbol{\Phi}^T dz, \tag{3.2.9}$$

$$\mathbf{B} = \left(\boldsymbol{\Phi}\boldsymbol{\Phi}^T\right)_{z=-H} + \left(\int_{-H}^{0} \boldsymbol{\Phi}_z\boldsymbol{\Phi}^T dz\right). \tag{3.2.10}$$

Both the (2D/3D) near-field model and the 1D far-field model make use of the same discretization (with $\boldsymbol{\Phi}(z)$ as the basis function vector) in the z direction.

3.3 Near field: Integration by parts in x, y directions

For the near field region, regular finite elements are used in the x (and y) directions. Thus weak form of the semi-discrete form of the governing equation (3.2.8) is obtained by appropriate integration by parts in x (and y) directions.

Integration by parts of the first term of (3.2.8) w.r.t x yields,

$$-\int_{-L/2}^{L/2} \delta\bar{u}\left(\mathbf{A}\frac{\partial}{\partial x}\boldsymbol{\Sigma}_1\right)dx = -\left(\delta\bar{u}\left[\mathbf{A}\boldsymbol{\Sigma}_1\right] - \int_{-L/2}^{L/2} \mathbf{A}\boldsymbol{\Sigma}_1 \frac{\partial\delta\bar{u}}{\partial x}dx\right). \tag{3.2.11}$$

Integration by parts in the y direction, for the second term of (3.2.8) takes a similar form:

$$-\int_{-B/2}^{B/2} \delta\bar{u}\left(\mathbf{A}\frac{\partial}{\partial y}\boldsymbol{\Sigma}_2\right)dy = -\left(\delta\bar{u}\left[\mathbf{A}\boldsymbol{\Sigma}_2\right] - \int_{-B/2}^{B/2} \mathbf{A}\boldsymbol{\Sigma}_2 \frac{\partial\delta\bar{u}}{\partial y}dy\right), \tag{3.2.12}$$

where the domain in x direction is assumed to span a length of L from $-\frac{L}{2}$ to $\frac{L}{2}$ and a breadth of B from $-\frac{B}{2}$ to $\frac{B}{2}$ in the y direction.

The system is then discretized in x and y directions using standard FEM along with PMDL.

3.4 Boundary Tractions

The traction at the boundaries arises from evaluating the $\left[\mathbf{A}\boldsymbol{\Sigma}_i\right]$ term in each of the equations (3.2.11) and (3.2.12). While the former gives the traction on the x boundaries the latter provides the tractions on the y boundaries.

Without loss of generality, let $\boldsymbol{\Sigma} = \begin{Bmatrix} \tau_1 \\ \tau_2 \end{Bmatrix}$ be the stresses for an element with two nodes in the vertical direction. Using linear elements in z direction with midpoint integration results in:

$$\mathbf{A} = \int_{-\Delta z}^{0} \boldsymbol{\Phi}\boldsymbol{\Phi}^T dz = \frac{\Delta z}{4}\begin{bmatrix} 1 & 1 \\ 1 & 1 \end{bmatrix}, \tag{3.3.1}$$

where Δz is the height of the element under consideration.

For a given element, the nodal forces P_i take the form,

$$\begin{Bmatrix} P_1 \\ P_2 \end{Bmatrix} = \mathbf{A}\boldsymbol{\Sigma}\Big|_{element} = \frac{\Delta z_i}{4}\begin{bmatrix} 1 & 1 \\ 1 & 1 \end{bmatrix}\begin{Bmatrix} \tau_1 \\ \tau_2 \end{Bmatrix}. \tag{3.3.2}$$

If there are $n+1$ nodes and corresponding values of stresses such that,

$$\boldsymbol{\Sigma} = \begin{Bmatrix} \tau_1 \\ \tau_2 \\ \vdots \\ \tau_{n+1} \end{Bmatrix}, \tag{3.3.3}$$

the contribution due to midpoint integrated traction from can be written as:

$$\mathbf{P} = \begin{Bmatrix} \left(\tau_1 + \tau_2/4\right)\Delta z_1 \\ \left(\tau_1 + \tau_2/4\right)\Delta z_1 + \left(\tau_2 + \tau_3/4\right)\Delta z_2 \\ \left(\tau_2 + \tau_3/4\right)\Delta z_2 + \left(\tau_3 + \tau_4/4\right)\Delta z_3 \\ \vdots \end{Bmatrix}. \tag{3.3.4}$$

This can be done for all three directions with each boundary consisting of three stress components as illustrated in Figure 3-4.

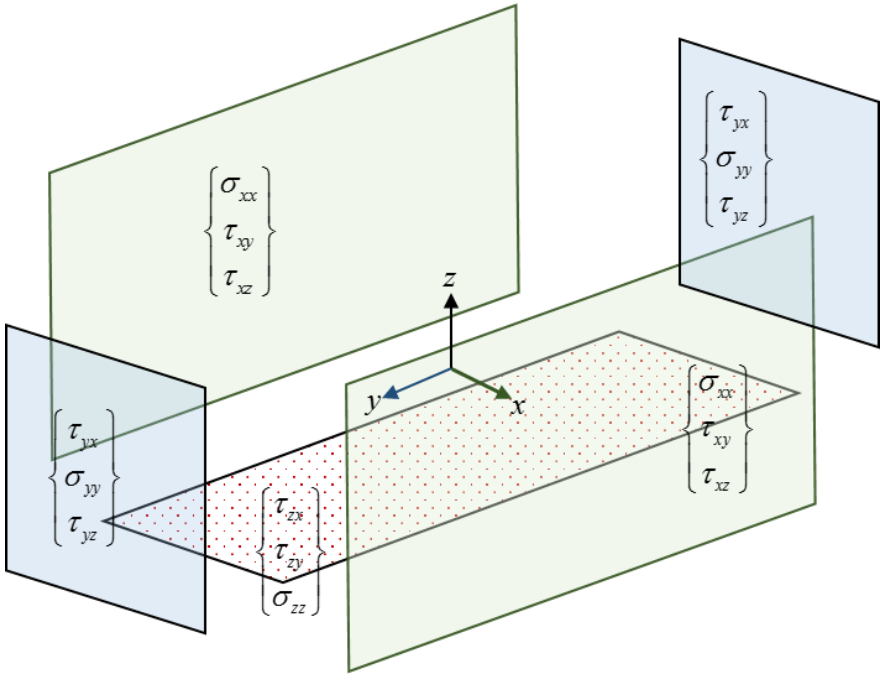

Figure 3-4 Exploded view of a 3D domain showing stresses on the boundaries with free top surface

3.5 Solution in the Exterior: Crank-Nicolson Method Consistent with Semi-discretization

The traction specification outlined in Section 3.4 makes use of the stresses at the nodes along the vertical direction to compute the traction acting on a boundary. Thus it is crucial to arrive at the correct values of displacements and stresses at the nodes, especially when unconventional discretization such as CFEM is used.

One way to ensure consistency would be to use the FE stiffness of the layer for the exterior solution. But the exterior problem is not a boundary value problem but an initial value problem (deconvolution) which requires a propagator matrix approach in the z direction. As already described one such deconvolution would be the Crank-Nicolson method. The displacement and stresses in the vertical direction are computed by marching in space in the vertical z direction, following (2.1.13):

$$\left[\frac{1}{\Delta z}\mathbf{I}_2 + \frac{1}{2}\mathbf{A}\right]\mathbf{p}^{n+1} = \left[\frac{1}{\Delta z}\mathbf{I}_2 - \frac{1}{2}\mathbf{A}\right]\mathbf{p}^{n}, \tag{3.4.1}$$

where $\mathbf{p} = \begin{Bmatrix} u \\ \tau \end{Bmatrix}$. The initial value at the free field is prescribed using $\mathbf{p}_0 = \begin{Bmatrix} u_0 \\ \tau_0 \end{Bmatrix}$ obtained from the free field ground motion. For a free surface, $\tau_0 = 0$.

Since the deconvoluted values are required at the nodes in the vertical direction that are consistent with the vertical discretization in the interior, the element lengths used in the Crank-Nicolson approach must be consistent with the vertical lengths of near-field elements which includes CFEM.

3.5.1 CFEM in the Interior

No excitation occurs inside the layers and hence in the z direction CFEM is employed in the interior for the layers that do not contain the structure of interest. The model schematic is illustrated in Section 2.3.4. The mesh in the vertical direction bent into complex plane, with linear interpolation and midpoint integration utilized in that direction (Section 2.3).

3.5.2 Consistent CFEM in the exterior (Crank Nicolson method with consistent complex valued steps)

If only FEM were used in the z direction, in the limit, the discrete approximation converges to the continuous case. However, the usage of CFEM implies that the developed stresses and displacement at the nodes must be consistent and equivalent with the modified mesh discretization.

In the z direction, the weak form of the equation (3.2.1) reduces to

$$\int \delta u \left(-\frac{\partial}{\partial z} G \frac{\partial u}{\partial z} - \rho \omega^2 u \right) dz = \sigma. \tag{3.4.2}$$

Using Galerkin approximation with semi-discretization, this is of the form

$$\left[\int \mathbf{\Phi}_z \mathbf{\Phi}_z^T dz + \lambda \int \mathbf{\Phi} \mathbf{\Phi}^T dz \right] \mathbf{U} = \mathbf{\Sigma}. \tag{3.4.3}$$

Evaluating the stiffness relation for a single element in the vertical direction with *linear shape functions and mid-point integration* we have,

$$\begin{Bmatrix} -\tau_1 \\ \tau_2 \end{Bmatrix} = \left(\frac{1}{\Delta z_i} \begin{bmatrix} 1 & -1 \\ -1 & 1 \end{bmatrix} + \frac{\lambda \Delta z_i}{4} \begin{bmatrix} 1 & 1 \\ 1 & 1 \end{bmatrix} \right) \begin{Bmatrix} u_1 \\ u_2 \end{Bmatrix}. \tag{3.4.4}$$

Using $\bar{\tau} = \frac{\tau}{\lambda}$, the above equation can be written in the propagator matrix form as,

$$\begin{Bmatrix} \frac{u_2 - u_1}{\Delta z_i} \\ \frac{\bar{\tau}_2 - \bar{\tau}_1}{\Delta z_i} \end{Bmatrix} = \begin{bmatrix} 0 & \sqrt{\lambda} \\ \sqrt{\lambda} & 0 \end{bmatrix} \begin{Bmatrix} \frac{u_2 + u_1}{2} \\ \frac{\bar{\tau}_2 + \bar{\tau}_1}{2} \end{Bmatrix}, \tag{3.4.5}$$

which can be written as

$$\frac{\partial}{\partial z} \begin{Bmatrix} u \\ \bar{\tau} \end{Bmatrix} = \mathbf{P}_i \begin{Bmatrix} u_{mid} \\ \bar{\tau}_{mid} \end{Bmatrix}. \tag{3.4.6}$$

This is equivalent to the *Crank Nicolson propagator matrix* formulation (see Section 2.1). This link provides the crucial basis for transferring information from the far-field deconvolution model to the near field interior domain.

Essentially, the Crank Nicolson method with propagator matrix is *equivalent* with (FEM+CFEM discretization) and mid-point integrated traction. The main feature is that, here the Crank-Nicolson method marches through depth, using element lengths that are *consistent* with FEM and CFEM, i.e., the lengths used for deconvolution are real valued in the FEM region and complex valued in CFEM region.

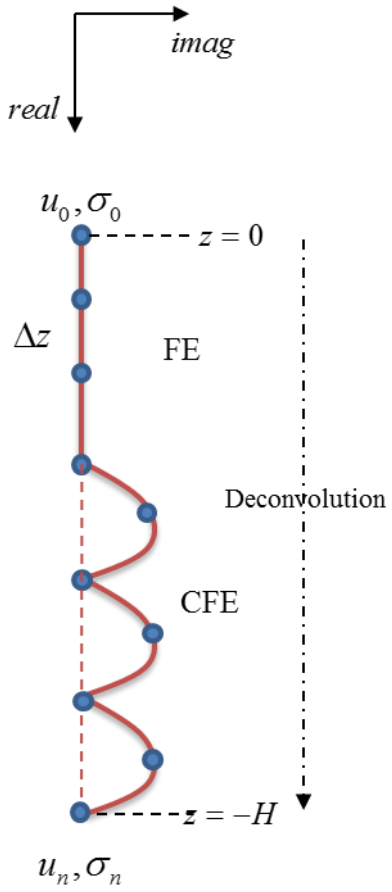

Figure 3-5 Illustration of consistent deconvolution

3.6 Solution in the Interior: Scattering Formalism

For the solution in the interior (near field), the 2D/3D model is provided with absorbing boundaries. In this thesis, we employ PMDL as the absorbing outer layers for the interior (see Section 2.2). The resulting system is depicted in Figure 3-6.

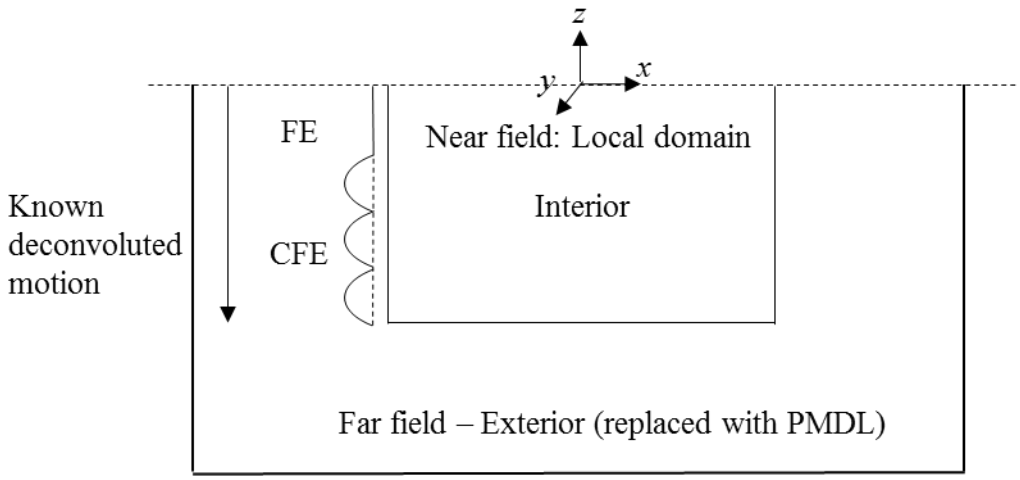

Figure 3-6 Schematic for scattering formalism

The goal now is to solve for the soil-structure interaction occurring in the interior region. Let the final solution for displacement be denoted by $\mathbf{u}$. The displacements obtained through the Crank Nicolson approach (solution in the exterior) gives the solution in the far-field, i.e. the incident wave-field denoted by $\mathbf{u}^I$. The consistent tractions prescribed on the boundary, as obtained from Section 3.4, be noted by $\mathbf{P}$.

For sake of illustration, a 1-D diagram (Figure 3-7) is used to depict the entire system, but the formulations are generic and hold true for 2D and 3D settings. The exterior, boundary and interior are denoted by subscripts e, b and i respectively.

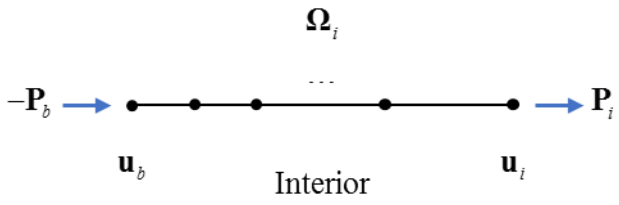

Figure 3-7 Domain depicting the interior

From Figure 3-7, the interior equilibrium equations can be written as,

$$\begin{bmatrix} \mathbf{K}_{ii} & \mathbf{K}_{ib} \\ \mathbf{K}_{bi} & \mathbf{K}_{bb} \end{bmatrix} \begin{Bmatrix} \mathbf{u}_i \\ \mathbf{u}_b \end{Bmatrix} = \begin{Bmatrix} \mathbf{P}_i \\ -\mathbf{P}_b \end{Bmatrix}, \tag{3.5.1}$$

where $\mathbf{K}$ refers to the dynamic stiffness matrix.

One way to solve the system would be to split the solution into incident and scattered wave fields. Let the scattered displacement be denoted by $\mathbf{u}^S$ and corresponding traction by $\mathbf{P}^S$. The scattered wave field satisfies the radiation boundary condition. This means that the waves must be purely outgoing and the exterior mesh modeled cannot have any incident excitation

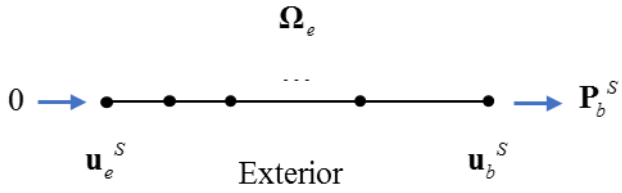

Figure 3-8 Scattered wave field in the exterior

The equation for the scattered wave field now becomes,

$$\begin{bmatrix} \overline{\mathbf{K}}_{bb} & \mathbf{K}_{be} \\ \mathbf{K}_{eb} & \mathbf{K}_{ee} \end{bmatrix} \begin{Bmatrix} \mathbf{u}_b^S \\ \mathbf{u}_e^S \end{Bmatrix} = \begin{Bmatrix} \mathbf{P}_b^S \\ 0 \end{Bmatrix}. \tag{3.5.2}$$

Using dynamic condensation we have,

$$\mathbf{P}_b^S = \left[\overline{\mathbf{K}}_{bb} - \mathbf{K}_{be} \left(\mathbf{K}_{ee} \right)^{-1} \mathbf{K}_{eb} \right] \mathbf{u}_b^S. \tag{3.5.3}$$

Using $\mathbf{u}_i = \mathbf{u}_i^I + \mathbf{u}_i^S$ and $\mathbf{u}_b = \mathbf{u}_b^I + \mathbf{u}_b^S$ and $\mathbf{P}_b = \mathbf{P}_b^I + \mathbf{P}_b^S$ we have,

$$\begin{Bmatrix} \mathbf{P}_i \\ -\mathbf{P}_b^I \end{Bmatrix} - \begin{bmatrix} \mathbf{K}_{ii} & \mathbf{K}_{ib} \\ \mathbf{K}_{bi} & \mathbf{K}_{bb} \end{bmatrix} \begin{Bmatrix} \mathbf{u}_i^I \\ \mathbf{u}_b^I \end{Bmatrix} = \begin{bmatrix} \mathbf{K}_{ii} & \mathbf{K}_{ib} \\ \mathbf{K}_{bi} & \overline{\mathbf{K}}_{bb} - \mathbf{K}_{be} \left(\mathbf{K}_{ee} \right)^{-1} \mathbf{K}_{eb} \end{bmatrix} \begin{Bmatrix} \mathbf{u}_i^S \\ \mathbf{u}_b^S \end{Bmatrix}. \tag{3.5.4}$$

The left hand side of (3.5.4) can be explicitly calculated from the deconvoluted incident wave field, and applied as tractions to determine $\mathbf{u}^S$.

While the scattered formalism described above applies to linear systems, SSI problems involve *non-linear* interiors, necessitating a formulation in terms of total displacement. Thus, rewriting (3.5.2) with $\mathbf{P}_b^S = \mathbf{P}_b - \mathbf{P}_b^I$ and $\mathbf{u}_b^S = \mathbf{u}_b - \mathbf{u}_b^I$ we have,

$$\begin{bmatrix} \overline{\mathbf{K}}_{bb} & \mathbf{K}_{be} \\ \mathbf{K}_{eb} & \mathbf{K}_{ee} \end{bmatrix} \begin{Bmatrix} \mathbf{u}_b \\ \mathbf{u}_e^S \end{Bmatrix} = \begin{Bmatrix} \mathbf{P}_b - \mathbf{P}_b^I + \overline{\mathbf{K}}_{bb} \cdot \mathbf{u}_b^I \\ \mathbf{K}_{eb} \cdot \mathbf{u}_b^I \end{Bmatrix}. \tag{3.5.5}$$

Note that in the second equation of (3.5.5), the exterior denoted by e can be further split into e_1 (first layer of exterior nodes) and e_r (rest of the exterior nodes).

Assembling (3.5.5) with (3.5.1) and setting $\mathbf{P}_i = 0$, the final formulation takes the form,

$$\begin{bmatrix} \mathbf{K}_{ii} & \mathbf{K}_{ib} & 0 & 0 \\ \mathbf{K}_{bi} & \mathbf{K}_{bb} + \overline{\mathbf{K}}_{bb} & \mathbf{K}_{be_1} & 0 \\ 0 & \mathbf{K}_{e_1 b} & \mathbf{K}_{e_1 e_1} & \mathbf{K}_{e_1 e_r} \\ 0 & 0 & \mathbf{K}_{e_r e_1} & \mathbf{K}_{e_r e_r} \end{bmatrix} \begin{Bmatrix} \mathbf{u}_i \\ \mathbf{u}_b \\ \mathbf{u}_{e_1} \\ \mathbf{u}_{e_r} \end{Bmatrix} = \begin{Bmatrix} 0 \\ -\mathbf{P}_b^I + \overline{\mathbf{K}}_{bb} \cdot \mathbf{u}_b^I \\ \mathbf{K}_{e_1 b} \cdot \mathbf{u}_b^I \\ 0 \end{Bmatrix}. \tag{3.5.6}$$

The only unknowns in the right hand side of equation(3.5.6) are $\mathbf{u}_b^I$ and the effective forces $\mathbf{P}_b^I$, acting on the boundary nodes, which are computed as discussed in Section 3.4.

3.7 Summary of the procedure

1) Discretize the entire domain using finite elements. Interior discretization follows regular FE formulation.

2) Apart from the layers containing the structure of interest, CFEM is used for the layers in vertical direction.
3) The exterior is efficiently modeled using PMDL.
4) The stresses $\boldsymbol{\tau}_b^I$ and displacements $\mathbf{u}_b^I$ are calculated at the boundary nodes from the incident wave field. This is done by consistent CN deconvolution of free field ground motion.
5) Tractions are specified at the boundary nodes, consistent with CFEM.
6) The system is solved for the displacement response using the scattering formalism.

3.8 Application to SSI

3.8.1 Anti-plane shear

Anti-plane shear deformation occurs in the form of vertically propagating shear horizontal (SH) waves. For a 2D domain in the $x-z$ plane, the incident wave would have a displacement component u_y and a shear stress component τ_{zy} (along with its complementary shear τ_{yz}). For this case, the incident wave field and the stresses are a function of only the depth (z). The traction in Equation (3.5.6) acts on the surface of the side boundaries and is of the form $\frac{\partial}{\partial x}\left(u_y\right)$. This dependence of u_y only on z implies that the traction terms on the sides go to zero, and hence the traction at the side boundaries do not enter into the formulation, thus simplifying the problem. However, the traction at the bottom boundary does enter the formulation and can be computed from the constant value of stress obtained at the bottom boundary via deconvolution.

3.8.2 Plane strain

Plane strain response arises out of incident waves that are vertically propagating shear vertical (SV) waves. In this case, for a 2D domain in the $x-z$ plane, the incident wave has a displacement component u_x and a shear stress component τ_{xz} (along with its complementary shear τ_{zx}). u_x is a function of x , which implies that traction is present in the side boundaries. This is crucial, as it implies that the traction so obtained must be consistent with the CFEM used on the side boundaries. To this end, the traction specification developed earlier based on mid-point integration ensures that the traction specified at the nodes are correct and consistent with CFEM.

The traction at the bottom boundary is similar to the case of Anti-plane shear deformation, i.e. it is obtained from the uniform stress computed at the bottom boundary.

4 NUMERICAL EXAMPLES

4.1 Verification of the approach

To verify the developed methodology, vertically incident shear wave is input onto a homogenous soil half-space. The half space is devoid of any scatterer and has a global free field motion of unit amplitude in the y direction for the case of anti-plane shear and in x direction for the case of plane strain.

For a given frequency ω and a soil of shear wave velocity c_s the wavenumber of the incident wave in the vertical (z) direction is $l = \frac{\omega}{c_s}$. Hence the incident wave is of the form $\cos(lz)$ and invariant in x direction.

This exact solution is computed in the domain and compared with the solution obtained from the developed finite element approach. The relative error is examined with increasing refinement for both plane strain and anti-plane shear. In both cases, the computed solution is found to converge to the exact solution upon refinement, as illustrated in Figure 4-1. Second order convergence is observed as expected, due to the use of regular linear finite elements.

For the convergence study, a frequency of 10 radians per second, a density of 1800 kg/m^3, shear modulus of 4 MPa and a Poisson's ratio of 0.25 was used. The input is obtained from deconvolution of unit amplitude free surface motion in the horizontal direction.

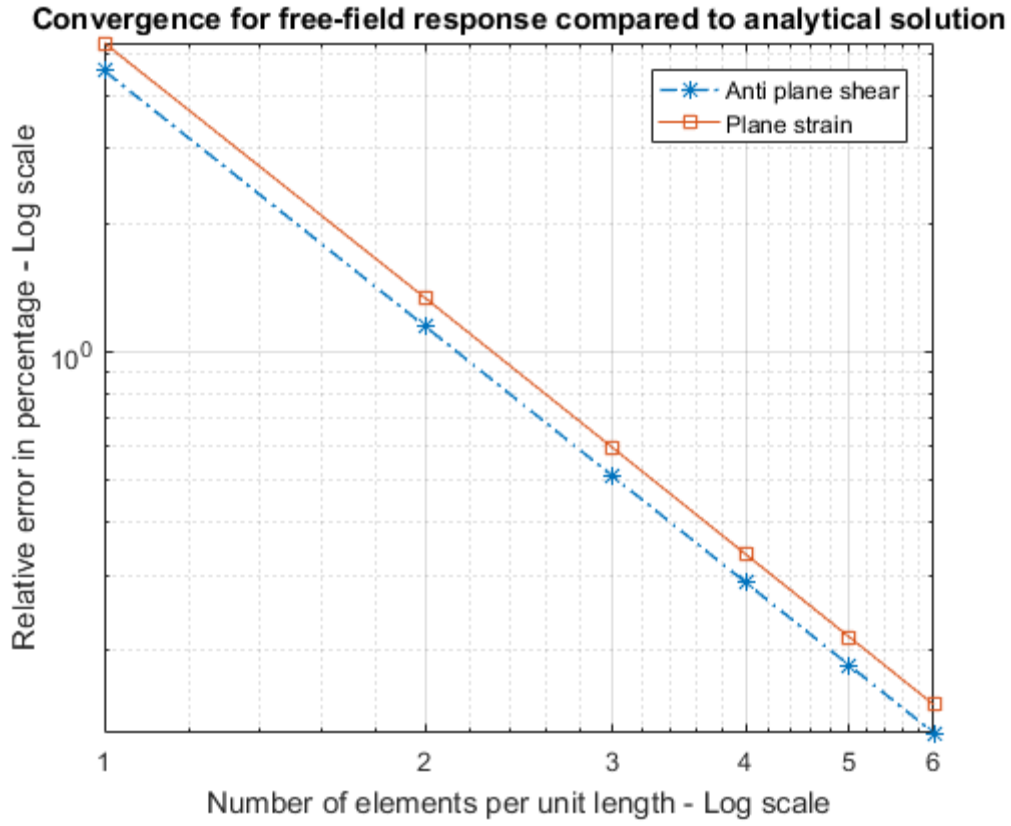

Figure 4-1 A Log plot of the convergence

4.2 Response amplification in Anti-plane shear

A structure with its base-mat resting on a three-layer soil is analyzed in anti-plane shear and compared with the response amplification of the same structure resting on homogenous soil half-spaces of different velocities. The structure is idealized as a rectangular domain with geometric and material properties shown in

Table 4-1. The base-mat dimensions and properties are shown in

Table 4-2, while the properties of soil layers are shown in Table 4-3.

Table 4-1 Structure dimensions and properties

Length	10 m
Height	20 m
G (shear modulus)	50 MPa
ρ (Density)	2000 kg/m^3

Table 4-2 Base-mat dimensions and properties

Length	15 m
Height	1.5 m embedded in soil
G (shear modulus)	10 GPa
ρ (Density)	2500 kg/m^3

Table 4-3 Soil layers

	Depth in (m)	C_s in m/s (Shear wave velocity)	ρ in (kg/m^3)
Layer 1	50	300	1800
Layer 2	150	500	1800
Layer 3	300	1000	1800
Bedrock	Halfspace	4000	2700

The input motion is a unit amplitude displacement at the surface. Six PMDL layers are used on either side and at the bottom, with thicknesses determined from Equation (2.2.1). Given the expected high accuracy with 6 PMDL layers the computational domain is restricted to the length of the base mat.

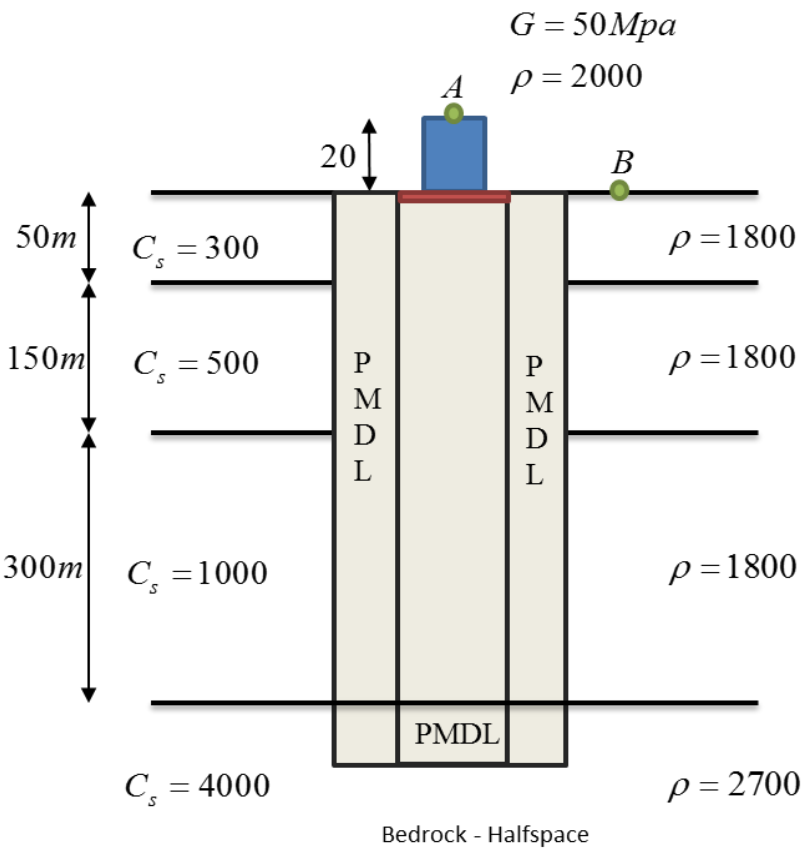

Figure 4-2 Schematic of the three layered soil profile

The goal of the analysis is the amplification factor, defined as the ratio $|u_A/u_B|$, where u_A is the displacement at point A at the top of the structure and u_B is the surface displacement in the far field. Figure 4-3 illustrates the amplification factor of the three layered soil system compared with homogenous soil profiles of different shear wave velocities. The amplification factor is as expected, with a peak near 0.5 seconds for the homogenous soil profiles. Increase in shear wave velocity resulted in greater amplification and reduction in fundamental time period, conforming to theoretically expected behavior. For the three-layer system, three

distinct peaks are observed consistent with the existence of three distinct layers, but the overall effect has resulted in a decreased maximum amplification.

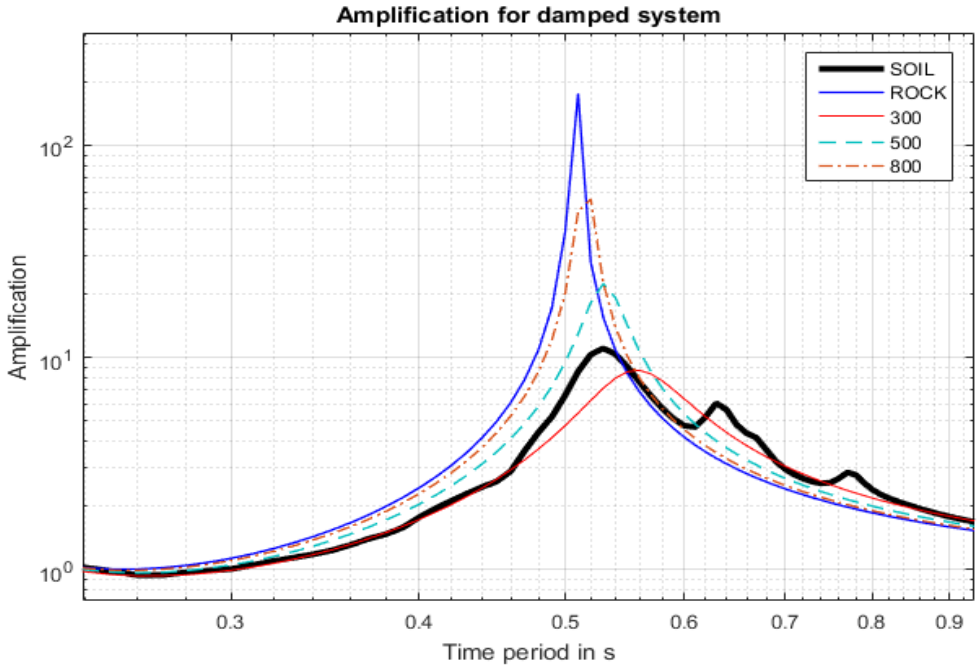

Figure 4-3 Amplification response plot

4.2.1 Performance of CFEM

For this three-layer soil strata, the model making use of Complex Finite elements for the layers is compared against a model comprising entirely of finite elements. Convergence analysis is performed in terms of the number of discretization layers in the vertical direction to achieve a target relative error of 1%. The number of finite elements in the horizontal x direction was kept the same (100) for both cases. Figure 4-4 shows a very close match of the converged plots. From

Table 4-4, it is clear that CFEM facilitates 6 fold reduction in number of elements used which is a significant reduction in computational cost, especially in three-dimensional settings.

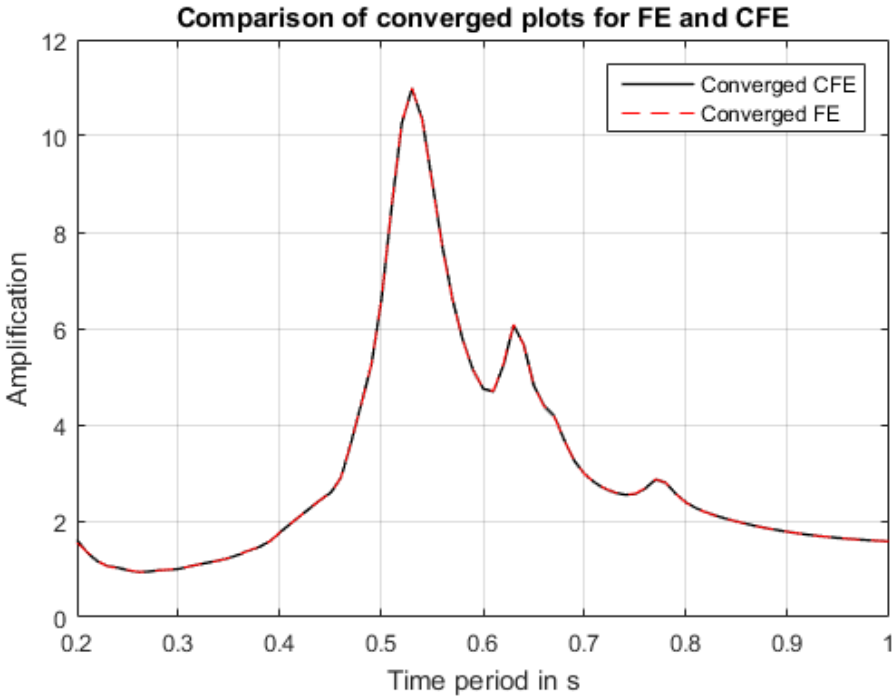

Figure 4-4 Converged FE and CFE plots for a target of 1% relative error

Table 4-4 Performance comparison - FE vs CFE

	Number of elements used in the vertical direction	**Number of elements Extrapolating to 3D problem**
Regular FE	120	1.2 million
Complex FE	18	180,000

4.3 Response amplification in plane strain

The system in the previous section is analyzed again, but now in plane strain, with a Poisson's ratio of 0.25 for all the layers. Figure 4-5 shows a marked difference in response characteristics compared to the case of anti-plane shear (Figure 4-3). Multiple resonant peaks are observed indicating the presence of multiple resonance modes under plane strain between 0.1 to 1

second. A closer look at the homogenous profile shows that the soils with higher shear wave velocity tend to have a greater amplification and at a time period lesser than that of lower velocity layers, which is expected and in agreement with the observation for the case of anti-plane shear. The amplification for multi-layered system is significantly different form that of homogenous soil profiles especially at higher frequencies. The sharp variations observed at higher frequency may be due to the presence of higher modes of vibration at larger frequencies and complex mode coupling that exists in plane strain.

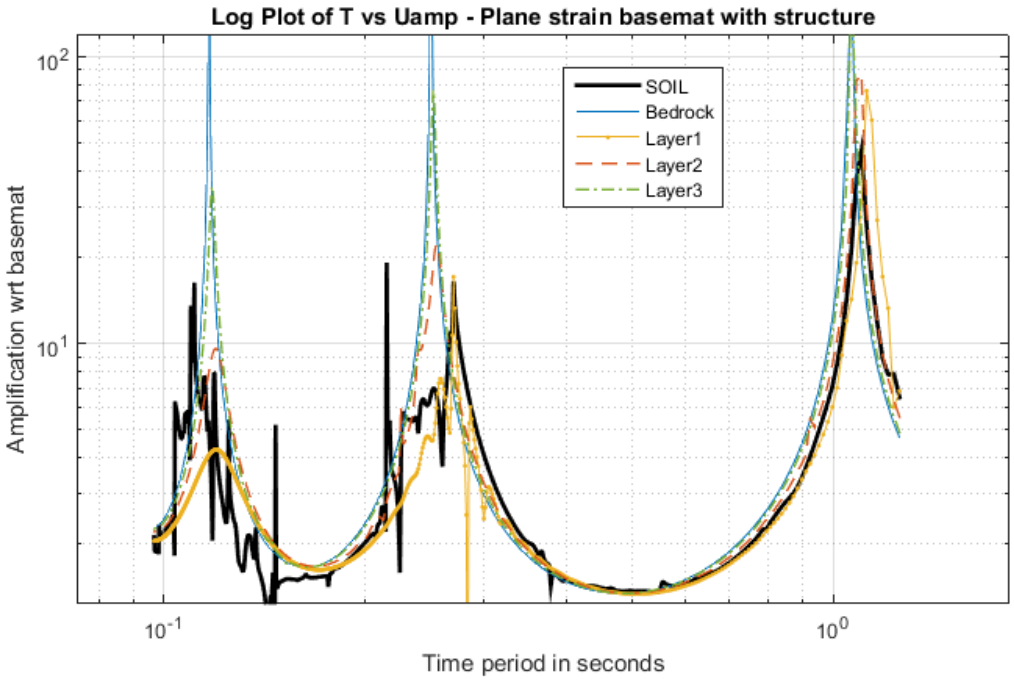

Figure 4-5 Plane strain response of structure

4.4 Response amplification for Realistic Soil-Structure System

For this example, a soil profile similar to an actual site in Taiwan is used (35). The soil profile data was obtained from borehole measurements and the paper (35) provides the geometry and geotechnical characterization of the site. The same structure with base-mat is used on this new soil-profile and the response obtained for the case of plane-strain and anti-plane shear. A comparison of performance of the CFEM based approach is carried out against a full FEM model. The structure and base-mat properties are the same as in

Table 4-1 and

Table 4-2. The soil characteristics are given in Table 4-5. The amplification factors are shown in Figure 4-6.

Table 4-5 Soil properties for five-layer system

Layers	Height in m	Shear Modulus in MPa
1	20	90
2	5	115
3	6	65
4	7	160
5	11	65
6	Halfspace	43.2 GPa
Density: (For all the soil layers)		1960 kg/m^3
Poisson's ratio: (For all soil layers)		0.25
Half-space density		2700 kg/m^3

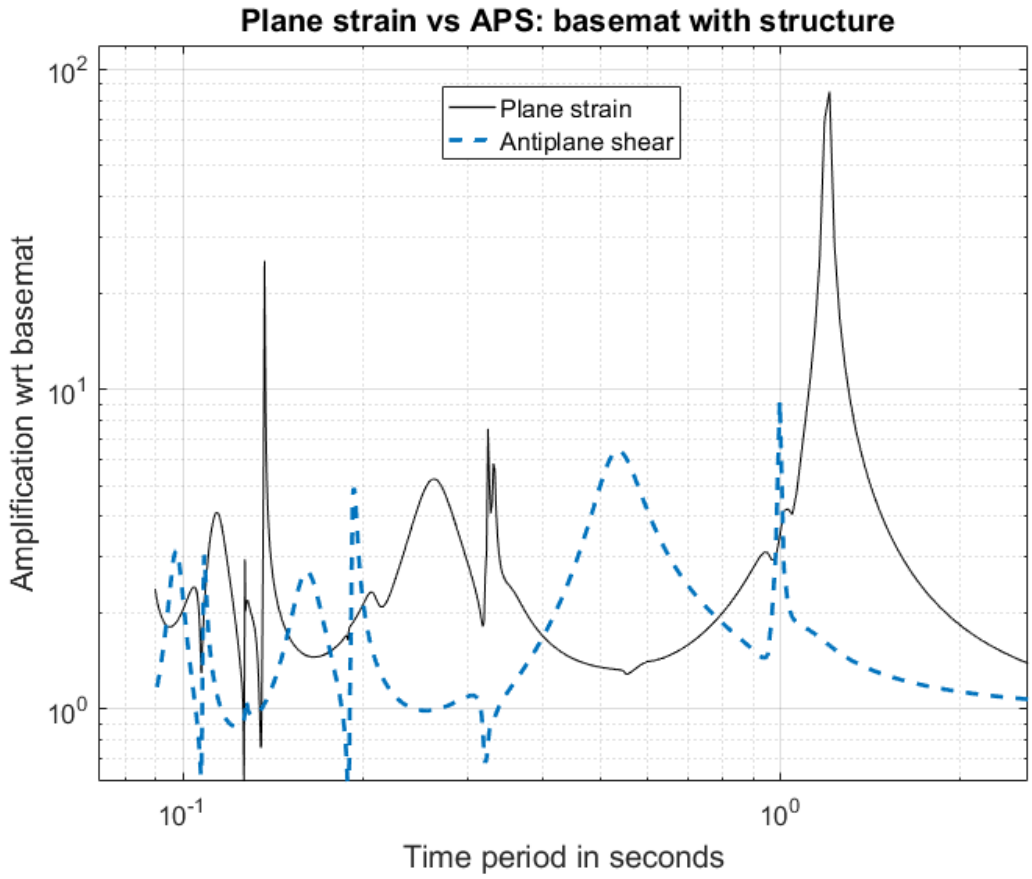

Figure 4-6 Five layered soil site - PS vs APS response

The anti-plane shear response, as denoted by the dashed line, is in stark contrast with the anti-plane response as seen in the previous example. One possible explanation for the behavior is that the soil layers in this example here have a sharply varying shear moduli in comparison with the previous example. The plane strain response is irregular and is distinctly higher in magnitude. As with the previous example, the resonant frequencies are different between plane-strain and anti-plane shear.

4.4.1 Performance Analysis: CFE vs FE - Example 2

Figure 4-7 and Figure 4-8 illustrate the fast convergence offered by CFEM, compared to slow algebraic convergence of FEM. The number of elements in the vertical direction required for CFEM is an order of magnitude less than FEM, while the error in CFEM is several orders of magnitude smaller, clearly illustrating the efficiency offered by CFEM.

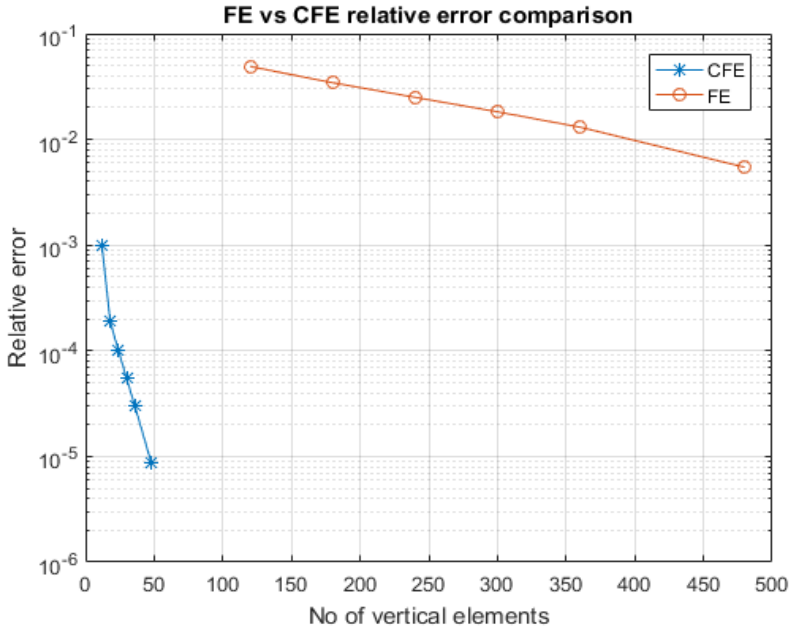

Figure 4-7 Antiplane shear - CFE performance

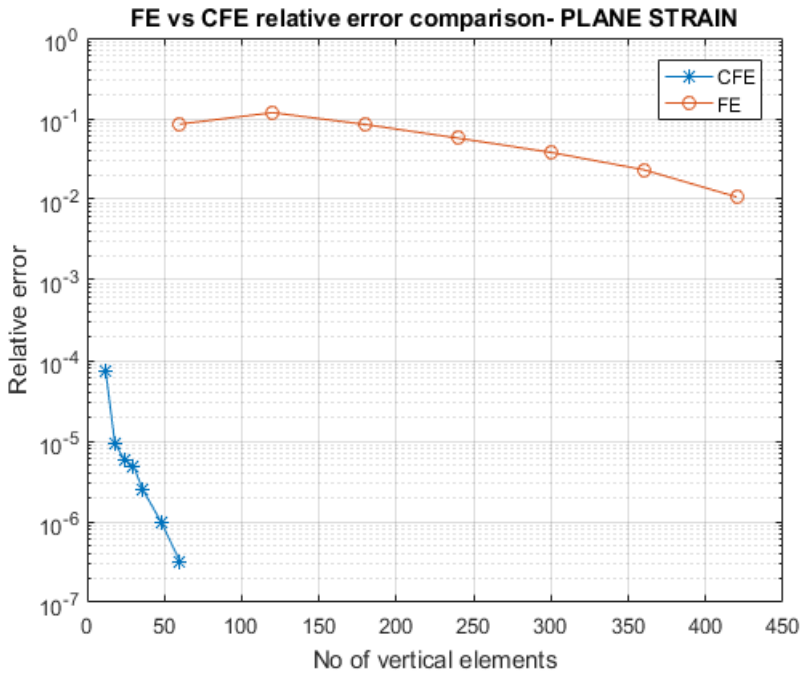

Figure 4-8 Plane strain - CFE performance

5 SUMMARY AND CONCLUSIONS

The proposed approach introduces complementing ideas for efficient analysis of soil-structure interaction that involve horizontally layered soil strata. These include: (a) Incorporating Complex-length Finite Element Method (CFEM), (b) devising a compatible Crank-Nicolson method for the exterior, and (c) a consistent procedure for transferring traction between global and local models. Based on numerical experiments, for practical error tolerance requirements, there is an order of magnitude reduction in number of elements used, resulting in significant savings over the existing techniques. The approach requires minimal modification to existing finite element code and the extension to 3D settings is straightforward. In fact, in 3D settings, the reduction in computational cost is expected to be even more significant. Possible areas of future research include extension to 3D, time-domain and irregularly layered soil profiles.

6 REFERENCES

1. Kramer SL. Geotechnical earthquake engineering. Pearson Education India; 1996.

2. Aki K, Richards PG. Quantitative seismology. ; 2002.

3. Mylonakis G, Gazetas G. Seismic soil-structure interaction: beneficial or detrimental? J Earthquake Eng. 2000;4(03):277-301.

4. Seed RB, Dickenson SE, Mok CM. Recent lessons regarding seismic response analysis of soft and deep clay sites. In: Technical Report NCEER. US National Center for Earthquake Engineering Research (NCEER); 1992. p. 131-45.

5. Zerva A, Petropulu AP, Bard P. Blind deconvolution methodology for site-response evaluation exclusively from ground-surface seismic recordings. Soil Dyn Earthquake Eng. 1999;18(1):47-57.

6. Arslan H, Siyahi B. A comparative study on linear and nonlinear site response analysis. Environ Geol. 2006;50(8):1193-200.

7. Motazedian D, Banab KK, Hunter JA, Sivathayalan S, Crow H, Brooks G. Comparison of site periods derived from different evaluation methods. Bulletin of the Seismological Society of America. 2011;101(6):2942-54.

8. Stewart JP, Fenves GL, Seed RB. Seismic soil-structure interaction in buildings. I: Analytical methods. J Geotech Geoenviron Eng. 1999;125(1):26-37.

9. Safak E. Discrete-time analysis of seismic site amplification. J Eng Mech. 1995;121(7):801-9.

10. Venture NCJ. Soil-structure interaction for building structures. NIST GCR. 2012:12-917.

11. Bielak J, Xu J, Ghattas O. Earthquake ground motion and structural response in alluvial valleys. J Geotech Geoenviron Eng. 1999;125(5):413-23.

12. Kim DK, Yun C. Earthquake response analysis in the time domain for 2D soil–structure systems using analytical frequency-dependent infinite elements. Int J Numer Methods Eng. 2003;58(12):1837-55.

13. Hisada Y. An efficient method for computing Green's functions for a layered half-space with sources and receivers at close depths. Bulletin of the Seismological Society of America. 1994;84(5):1456-72.

14. Davoodi M, Sadjadi M, Goljahani P, Kamalian M. Effects of Near-Field and Far-Field Earthquakes on Seismic Response of SDOF System Considering Soil Structure Interaction. 15th World Conference on Earthquake Engineering. Lisbon, Portugal; ; 2012.

15. Bao H, Bielak J, Ghattas O, Kallivokas LF, O'Hallaron DR, Shewchuk JR, et al. Large-scale simulation of elastic wave propagation in heterogeneous media on parallel computers. Comput Methods Appl Mech Eng. 1998;152(1):85-102.

16. Wolf JP. Dynamic soil-structure interaction. Prentice Hall int.; 1985.

17. Lysmer J, Tabatabaie-Raissi M, Tajirian F, Vahdani S, Ostadan F. SASSI. System for Analysis of Soil Structure Interaction, UC Berkeley, Dept.of Civil Engineering, Berkeley, CA. 1983.

18. Nie J, Braverman J, Costantino M. Seismic Soil-Structure Interaction Analyses of a Deeply Embedded Model Reactor–SASSI Analyses. NIST GCR. 2013.

19. Jeremić B, Tafazzoli N, Ancheta T, Orbović N, Blahoianu A. Seismic behavior of NPP structures subjected to realistic 3D, inclined seismic motions, in variable layered soil/rock, on surface or embedded foundations. Nucl Eng Des. 2013;265:85-94.

20. Bolisetti C. Site Response, Soil-Structure Interaction and Structure-Soil-Structure Interaction for Performance Assessment of Buildings and Nuclear Structures. Technical Report MCEER-15-0002. 2014.

21. Ashrafi SA, Abruzzo J, Singh P, Vahdani S. Seismic Soil-Structure Interaction Analysis for the Transbay Transit Center in San Francisco–Methodology. 15th World Conference on Earthquake Engineering; ; 2012.

22. Bielak J, Loukakis K, Hisada Y, Yoshimura C. Domain reduction method for three-dimensional earthquake modeling in localized regions, Part I: Theory. Bulletin of the Seismological Society of America. 2003;93(2):817-24.

23. Guddati M, Savadatti S. Efficient and accurate domain-truncation techniques for seismic soil-structure interaction. Earthquakes and Structures. 2012;3(3_4):563-80.

24. Hatzigeorgiou GD, Beskos DE. Soil–structure interaction effects on seismic inelastic analysis of 3-D tunnels. Soil Dyn Earthquake Eng. 2010;30(9):851-61.

25. Donikian R, Liu C, Liu Q, Clinch K. THREE-DIMENSIONAL SOIL-STRUCTURE INTERACTION ANALYSIS OF CUT-AND-COVER TUNNELS.

26. Humar JL, Bagchi A, Xia H. Frequency domain analysis of soil-structure interaction. Comput Struct. 1998;66(2):337-51.

27. Gupta S, Penzien J, Lin TW, Yeh CS. Three-dimensional hybrid modelling of soil-structure interaction. Earthquake Eng Struct Dyn. 1982;10(1):69-87.

28. Guddati MN, Lim KW, Zahid MA. Perfectly matched discrete layers for unbounded domain modeling. Computational Methods for Acoustics Problem, Saxe-Coburg Publications, Scotland. 2008:69-98.

29. Guddati MN, Lim K. Continued fraction absorbing boundary conditions for convex polygonal domains. Int J Numer Methods Eng. 2006;66(6):949-77.

30. Berenger J. A perfectly matched layer for the absorption of electromagnetic waves. Journal of computational physics. 1994;114(2):185-200.

31. Chew WC, Weedon WH. A 3D perfectly matched medium from modified Maxwell's equations with stretched coordinates. Microwave Opt Technol Lett. 1994;7(13):599-604.

32. Savadatti S, Guddati MN. Absorbing boundary conditions for scalar waves in anisotropic media. Part 1: Time harmonic modeling. Journal of Computational Physics. 2010;229(19):6696-714.

33. Guddati MN, Druskin V, Astaneh AV. Exponential Convergence through Linear Finite Element Discretization of Stratified Subdomains. arXiv preprint arXiv:1507.05038. 2015.

34. Vaziri Astaneh A, Guddati MN. Efficient computation of dispersion curves for multilayered waveguides and half-spaces. Comput Methods Appl Mech Eng. 2016;300:27-46.

35. Amorosi A, Annamaria DL, Boldini D. ADVANCED NUMERICAL APPROACHES TO THE SEISMIC SOIL AND STRUCTURAL RESPONSE ANALYSES. Cambridge UK: ; 2015.

7 APPENDICES

7.1 Appendix A - The link between DRM and SCM

The scattering formalism developed by (23, 32) and illustrated in Section 3.6, which has been extended to include CFEM layers will herein be referred to as Stiffness-Consistent Method or SCM in short (since the traction is consistent with the stiffness).

The Domain Reduction Method (DRM) is an alternate approach (22) to SCM. The basic idea of DRM involves calculating the effective forces in the nodes of the first band of elements outside the boundary. The approaches developed in this thesis can be combined with DRM used in place of SCM; in fact, this has been implemented and found to work well.

A comparison on the equations of the DRM and SCM formulations provides an interesting insight into the links between the two approaches. The general idea is that both the approaches essentially have the same basis, but approach the problem of obtaining effective forces in the local domain differently; this Appendix aims to illustrate this link.

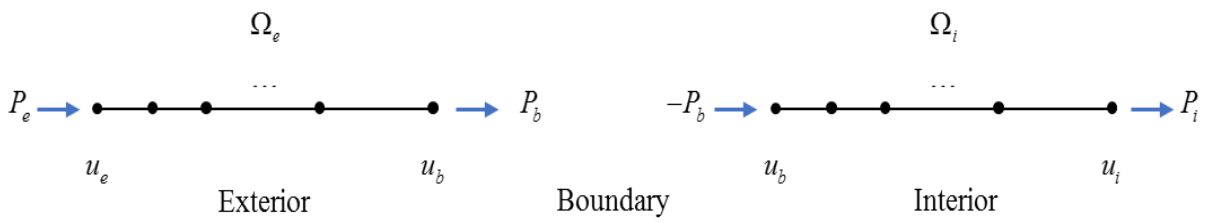

Figure 7-1 Domain depicting the exterior and interior separation

We limit the discussion to 1D setting for sake of simplicity, but the ideas are easily extended to higher dimensions.

From Figure 7-1, interior and exterior equilibrium equations can be written as,

$$\begin{bmatrix} K_{ii} & K_{ib} \\ K_{bi} & K_{bb} \end{bmatrix} \begin{Bmatrix} u_i \\ u_b \end{Bmatrix} = \begin{Bmatrix} P_i \\ -P_b \end{Bmatrix}, \text{ for } \Omega_i . \tag{6.1.1}$$

$$\begin{bmatrix} \overline{K}_{bb} & K_{be} \\ K_{eb} & K_{ee} \end{bmatrix} \begin{Bmatrix} u_b \\ u_e \end{Bmatrix} = \begin{Bmatrix} P_b \\ P_e \end{Bmatrix}, \text{ for } \Omega_e . \tag{6.1.2}$$

Subscripts b denotes boundary, i for interior and e for exterior nodes. K refers to the dynamic stiffness while P refers to the force vector.

7.1.1 The DRM Approach

DRM employs the fact that P_e (forcing in the exterior) is the same as P_e^I (incident forcing in the exterior).

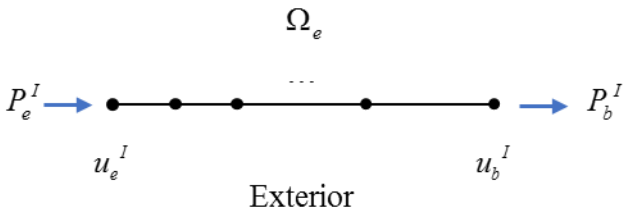

Figure 7-2 Incident wave field in scatter free exterior

Hence if there was just the global domain without any local features, the exterior Ω_e for the incident wave field, takes the following form:

$$\begin{bmatrix} \overline{K}_{bb} & K_{be} \\ K_{eb} & K_{ee} \end{bmatrix} \begin{Bmatrix} u_b^I \\ u_e^I \end{Bmatrix} = \begin{Bmatrix} P_b^I \\ P_e \end{Bmatrix}. \tag{6.1.3}$$

The DRM method makes use of the second equation in (6.1.3) to obtain,

$$P_e = K_{eb} u_b^{\ I} + K_{ee} u_e^{\ I}, \tag{6.1.4}$$

which when used in equation (6.1.2) leads to

$$\begin{bmatrix} \overline{K}_{bb} & K_{be} \\ K_{eb} & K_{ee} \end{bmatrix} \begin{Bmatrix} u_b \\ u_e \end{Bmatrix} = \begin{Bmatrix} P_b \\ K_{eb} u_b^{\ I} + K_{ee} u_e^{\ I} \end{Bmatrix}. \tag{6.1.5}$$

Using $u_e = u_e^{\ I} + u_e^{\ S}$, equation (6.1.5) becomes,

$$\begin{bmatrix} \overline{K}_{bb} & K_{be} \\ K_{eb} & K_{ee} \end{bmatrix} \begin{Bmatrix} u_b \\ u_e^{\ S} \end{Bmatrix} = \begin{Bmatrix} P_b - K_{be} u_e^{\ I} \\ K_{eb} u_b^{\ I} \end{Bmatrix}, \tag{6.1.6}$$

which when assembled with Ω_i equation (6.1.1) gives the full DRM formulation.

7.1.2 The SCM Approach

The key difference in SCM is that, instead of looking at scatter free incident wave field (6.1.3) SCM uses radiation boundary condition in the scattered exterior wave field. Due to radiation boundary condition, there is no forcing arising from the exterior. This provides the scattered wave field in the exterior as:

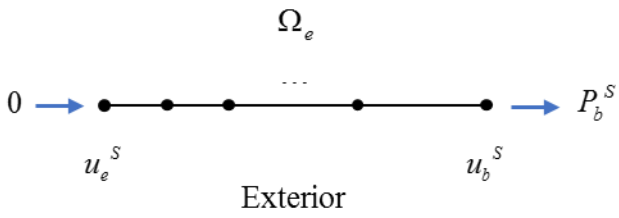

Figure 7-3 Scattered wave field in the exterior

The equation for the scattered wave field becomes,

$$\begin{bmatrix} \overline{K}_{bb} & K_{be} \\ K_{eb} & K_{ee} \end{bmatrix} \begin{Bmatrix} u_b{}^S \\ u_e{}^S \end{Bmatrix} = \begin{Bmatrix} P_b^S \\ 0 \end{Bmatrix}. \tag{6.1.7}$$

Note that the second equation of (6.1.7) is the same as the second equation of (6.1.5) with $u = u^I + u^S$. Rewriting (6.1.7) with $P_b^S = P_b - P_b^I$ and $u_b{}^S = u_b - u_b{}^I$ we have,

$$\begin{bmatrix} \overline{K}_{bb} & K_{be} \\ K_{eb} & K_{ee} \end{bmatrix} \begin{Bmatrix} u_b \\ u_e{}^S \end{Bmatrix} = \begin{Bmatrix} P_b - P_b^I + \overline{K}_{bb} \cdot u_b{}^I \\ K_{eb} \cdot u_b{}^I \end{Bmatrix}. \tag{6.1.8}$$

SCM proceeds to calculate P_b^I from the tractions on the boundary. For example, for the case of anti-plane shear, $P_b{}^I$ would be of the form:

$$P_b{}^I = G \frac{\partial \left(u_b{}^I \right)}{\partial \mathbf{n}}. \tag{6.1.9}$$

Assembling Equations (6.1.8) and (6.1.1) gives the full SCM formulation.

Comparing the SCM formulation in Equation (6.1.8) and the DRM formulation in Equation (6.1.6) we note that the difference is in the right hand side:

DRM: $-K_{be} u_e{}^I$

SCM: $-P_b^I + \overline{K}_{bb} \cdot u_b{}^I$

The first Equation in (6.1.3) gives the equivalence that

$$-K_{be} u_e{}^I = -P_b^I + \overline{K}_{bb} \cdot u_b{}^I \tag{6.1.10}$$

Hence both the methods are essentially equivalent approaches with the exception of the discretization error.